QUANTIFYING MENTHOL CONCENTRATION IN HUMAN URINE VIA GAS SENSING: POSSIBLE APPROACHES AND INITIAL FEASIBILITY

By

Jacob Brady

A capstone project submitted for Graduation with University Honors

May 5, 2021

University Honors
University of California, Riverside

APPROVED

Dr. Nosang Myung
Department of Chemical and Environmental Engineering

Dr. Richard Cardullo, Howard H Hays Jr. Chair
University Honors

Abstract

Interstitial cystitis is a medical condition involving chronic, painful inflammation of the urinary bladder that affects millions of Americans each year. Recent research identified (*l*)-menthol as a biomarker for interstitial cystitis, wherein interstitial cystitis patients had a reduced concentration of menthol present in their urine compared to healthy patients. The use of inexpensive chemiresistive gas sensors for quantifying menthol in the vapor headspace above a urine sample could offer multiple advantages over the currently used analytical instruments in terms of cost and portability. To evaluate the feasibility of quantifying menthol vapor in the headspace above a urine sample, several commercially sourced metal oxide-based gas sensors were exposed to menthol-air mixtures with concentrations of 0.0011, 0.12, 0.24, 0.36 and 0.48 ppm menthol. The voltage and resistance measurements obtained from the gas sensors were analyzed to quantify their menthol sensing characteristics. Several of the sensors responded to 0.12 ppm menthol and higher. The MICS 6814 and MICS 5524 sensors were identified as having the best menthol detection characteristics on the basis of highest linear sensitivity magnitude (MICS 6814: 0.971 ppm^{-1}) and lowest extrapolated lower limit of menthol detection (MICS 5524: 0.014 ppm). The implications of these results and potential future research directions in light of these results were also discussed.

Acknowledgements

I would like to extend my sincere thanks to my faculty mentor, Dr. Nosang Myung, for the professional support and guidance he has provided me since I first joined his research group in January 2019, including support and guidance connected to this project. I would like to acknowledge Dr. Thien-Toan Tran for his professional support and guidance, including his substantial contributions, feedback and assistance in planning experiments, collecting data and much more both in connection to this project and beyond it, especially during the COVID-19 pandemic. I must admit that I miss the crazy late nights of setting up experiments in the lab with Toan and Joseph pre-COVID.

I would also like to acknowledge the contributions of several students currently or formerly associated with Dr. Nosang Myung's group including Joseph Hart, Isaac Hong, Faraj Al-Badani, Suporna Paul and Bingxin Yang to various areas in Dr. Myung's group that exerted some influence on my capstone project. The connections I made, early experiences as a researcher I had and mentorship I received in Dr. Myung's group over the last two and half years are the three most rewarding things that I have gotten out of attending UC Riverside. I would not be pursuing a PhD after graduating from UC Riverside without the experiences that I had and the support I received from Dr. Myung and Dr. Tran.

Most of the funding for acquiring the materials and equipment used to conduct the experiments and collect data for this project was provided through Naval Sea Systems Command (NAVSEA) Corona, contract no. N6426719C0024.

Table of Contents

I. Introduction and Background Information

I.A Interstitial Cystitis and Menthol

The chemical structure of (*l*)-menthol is shown in **Figure 1**. (*l*)-menthol, hereafter referred to as menthol, is the naturally occurring enantiomer of menthol that is found in a few species in the mint plant family. Its chemical formula is $C_{10}H_{20}O$. It is notably used in cough drops, as a food additive and in other common consumer products to produce a minty flavor or "cooling" sensation when it comes into contact with skin or the mucus membranes inside one's mouth and throat.

Menthol has been recently identified as a biomarker for interstitial cystitis. Shahid et al. found that the concentrations of menthol in the urine of patients diagnosed with interstitial cystitis was significantly reduced compared to healthy controls,[1] which makes menthol a potentially useful detection target for diagnostic purposes. Interstitial cystitis is a disease characterized by chronic inflammation of the urinary bladder that causes pain and discomfort in those affected. This disease, the causes of which are still not completely clear, affects millions of Americans annually.[1]

I.B Project Motivation and Objectives

Shahid et al. used gas chromatography-mass spectrometry (GC-MS) to quantify the concentration of menthol in their urine samples.[1] GC-MS is a powerful tool that can very accurately quantify the concentration of a particular chemical in a given sample; however, GC-MS equipment is very expensive, requires advanced training to use and is limited to being used in a lab setting.

One possible alternative to using GC-MS equipment to quantify menthol concentrations in urine that addresses the shortcomings listed in the previous paragraph would be to sample and analyze the vapor headspace above a urine sample using an inexpensive, miniaturized gas sensor.

Since menthol is a volatile compound, a small quantity of the menthol dissolved in urine would be expected to vaporize into the headspace above the urine sample.

The original objective of my capstone project was to initiate an investigation into quantifying the concentration of menthol in a urine sample by evaluating the response characteristics of inexpensive commercially available and custom-made chemiresistive gas sensors exposed to the vapor headspace of an artificial urine mixture containing a dissolved quantity of menthol. The sensor responses were to be correlated to the liquid-phase concentration of dissolved menthol to see if detecting menthol in the vapor headspace was feasible. However, due to the limitations on laboratory access imposed as a result of the COVID-19 pandemic, the scope of data collected was narrowed somewhat so that only menthol vapor mixed with air was evaluated by commercially available gas sensors. Despite this limitation in scope, useful results regarding the feasibility of detecting and quantifying menthol vapor in air using commercially available gas sensors were still obtained.

I.C – Chemiresistive Gas Sensing Overview

Broadly, chemiresistive gas sensors operate by measuring the change in the electrical conductivity or resistance of a material that occurs because of a change in the composition of the gas that surrounds the material. The change in resistance can be correlated to the change in the composition of the surrounding gaseous environment under controlled conditions so that the change in the material's resistance can then be used to predict the gaseous environment's composition in a different environment.

The commercially available gas sensors which were evaluated in this project are listed in **Table 1**. Powdered and nanostructured semiconducting metal oxides are the functional materials

in these sensors. I will very briefly outline the most widely accepted mechanism that has been proposed for operation of metal oxides as a gas sensing material next, though I will refrain from going into excessive detail. Other references cover this topic in much more detail.[2–4]

When the semiconducting metal oxide is heated to a sufficiently high temperature (usually above 250°C or 300°C) in the presence of oxygen gas, some of the oxygen will bind to the surface of the metal oxide as an oxide, such as O_2^- or O^{2-}. Electrons are taken from the metal oxide itself during this process to form the oxides, and the removal of these electrons to form the absorbed oxides results in a change in the electrical conductivity of the metal oxide. Depending on the electrical properties of the specific metal oxide and the presence of additives, this can cause an increase or decrease in electrical conductivity to be observed. After a period of time, the conductivity of the metal oxide will reach a stable equilibrium value.

When a volatile organic compound (VOC), such as menthol, is then introduced into the environment around the metal oxide, it reacts with the absorbed oxides on the surface to form carbon dioxide, water and possibly other products. When the absorbed oxides are consumed, the VOC donates electrons back into the metal oxide, partially reversing the change in conductivity that was observed when the metal oxide was exposed to oxygen alone. Eventually, the conductivity of the metal oxide will reach a new equilibrium value.

A full discussion on the many different methods, modalities and molecular mechanisms of gas sensing is beyond the scope of this capstone. The interested reader is directed to *Chemical Sensors: An Introduction for Scientists and Engineers*,[5] which provides a broad, general introduction of gas sensing and chemical sensing in general, and *Metal Oxide Nanostructures as Gas Sensing Devices*,[6] which provides a good overview of gas sensing using different nanostructured metal oxides.

I.D Properties of Menthol and Calculating Gas Phase Concentrations

It is important to have some understanding of the physical and chemical properties of menthol for the purposes of gas sensing. The most relevant property of menthol for gas sensing is its vapor pressure, as this can be used to calculate the vapor-phase concentration of menthol above a solid sample of menthol.

Despite menthol being a solid at room temperature, it exerts a vapor pressure. That is, some solid menthol sublimates directly into the vapor phase, producing a noticeable mint-like smell. Quantifying this vapor pressure is important for designing the gas sensing experiments discussed later. Thus, data for the vapor pressure of solid (*l*)-menthol was reviewed and complied from recently published literature.[7] The literature data was then fit to an Antione equation (see section *III.A*) which relates the vapor pressure of menthol to the temperature over a narrow range of temperatures encountered during the experiments.

Given the vapor pressure of menthol, its concentration in the vapor phase on a molar basis can then be calculated using Raoult's and Dalton's laws. Raoult's law for a *pure* solid compound can be formulated as:

$$P_A = P_{vp,A} \quad (1)$$

In equation (1), P_A is the partial pressure of compound A in the vapor phase and $P_{vp,A}$ is the vapor pressure of compound A. This is essentially a statement of thermodynamic equilibrium between the vapor and solid phases that is valid at low (i.e. near atmospheric) pressures.[8]

Dalton's law relates the partial pressure of a compound in the vapor phase to its mole fraction:

$$P_A = y_A P \quad (2)$$

In equation (2), y_A is the mole fraction of component A in the vapor phase (moles A/moles gas) and P is the total pressure in the system.

Equations (1) and (2) can be combined and rearranged to yield the following useful relationship between vapor pressure, total pressure and mole fraction (concentration) in the gas phase:

$$y_A = \frac{P_{vp,A}}{P} \quad (3)$$

For most solid compounds, including menthol, the vapor pressure is typically much lower than the overall pressure, so y_A tends to be very small. Therefore, it is often convenient to multiply y_A by 10^6 or 10^9 to convert the vapor-phase concentration to parts per million (ppm) or parts per billion (ppb), respectively. Menthol concentrations in this paper are reported in ppm.

When a gas mixture containing a dilute concentration of component A with flow rate F_1 and concentration $y_{A,1}$ is mixed and diluted with a gas stream of flow rate F_2 containing no component A, the new total flow rate is $F_1 + F_2$ and the new concentration of component A is given by:

$$y_{A,2} = \frac{y_{A,1}F_1}{F_1+F_2} \quad (4)$$

This simple equation for calculating the new concentration of a dilute component after further dilution was used to calculate MFC (mass flow controller) flow rates as mentioned in section *II.C.*

II. Experimental Methods and Materials

II.A Sensor List

Nineteen commercially-available metal oxide-based gas sensors were evaluated in this experiment. **Table 1** lists the sensors that were evaluated. This table includes the name of the

sensor, a unique ten character alphanumeric identifier assigned to each individual sensor for tracking purposes and the name of the sensor manufacturer. Of the nineteen sensors evaluated, there are eleven unique sensors; the remaining eight are replicates of the eleven unique sensor models.

II.B Experimental Apparatus

From April through June 2019, an apparatus for generating and diluting mixtures of analyte and carrier gases for gas sensing experiments was designed and constructed by a few members of the Myung group. I contributed to both the design and physical construction of the apparatus along with Dr. Tran and a few other undergraduates. A general schematic of the apparatus is shown in **Figure 2**. In summary, a low flow rate of air (~5 sccm) was allowed to pass over a sample of solid menthol at an ambient temperature of about 25°C. The air/menthol mixture then mixed with air to dilute it once. The diluted menthol/air mixture was then split; a small quantity was diluted again by air and traveled to the individual gas sensors housed in plastic 3D-printed chambers at a total flow rate of 500 sccm, while the excess was exhausted into a fume hood. The air/menthol mixture which passed over the sensors was also exhausted into a fume hood. MFCs, or mass flow controllers, purchased from Alicat Scientific were used to control the flow rates and direction of flow by allowing gas to flow down a pressure gradient at a controlled rate. Most of the tubing which carried the different gas mixtures in the apparatus was small-diameter stainless steel tubing purchased from McMaster Carr, although some flexible Teflon tubing was used for components that had to regularly be modified or moved around, such as the 3D-printed sensor chambers.

The gas sensors themselves were housed in custom 3D-printed chambers which isolated them from the lab atmosphere so as to avoid outside contamination and ensure that the responses

of the sensors were only caused by menthol exposure. Sensor-specific circuit boards and Arduino microcontrollers were used to connect the sensors to a laptop so resistance measurements and other data could be read from them in a LabVIEW program. I did not contribute much to the design of the 3D-printed chambers, the electrical wiring of the sensors or the development of the LabVIEW programs; these tasks were primarily done by Dr. Tran and other undergraduate students in the lab.

It should also be noted that menthol was not the only analyte used in this apparatus. The apparatus was used to accommodate many different analytes from other projects, of which menthol was only one.

II.C – Gas Exposure Experiment Design

The analyte is the gaseous component to be detected by a gas sensor and typically makes up only a small portion of the total gas flow, while the carrier is the "background" gas that makes up most of the total gas flow. For this project, the analyte was menthol and the carrier gas was synthetic dry air (a mixture of approximately 79% nitrogen and 21% oxygen) that came from a pressurized gas tank.

Table 2 summarizes the sequence of steps in the gas sensing experiment. Initially, the system described in section *II.A* was purged with air for 36 hours to remove any lingering contaminants from previous experiments and allow the sensors to reach a baseline resistance. Next, the sensors were exposed to 0.0011, 0.12, 0.24, 0.36 and 0.48 ppm of menthol in air for one hour each, followed by four hours of purging with air to reset the sensors to their baselines. The sensors were exposed to each menthol concentration three times, resulting in a total experiment duration of 111 hours (about five days).

The flow rates of the MFCs required to obtain specific menthol concentrations via dilution were calculated in advance using equation (4) and supplied to a LabVIEW program on a laptop which controlled the MFC flow rates. The maximum flow rate through any one MFC was limited to 500 sccm, and the minimum flow rate that could be reliably obtained was 1 sccm. The flow rates of the MFCs were also set such that the total flow rate of gas delivered to the sensors remained constant for the duration of the experiment. This condition set on the total flow rate delivered to the sensors was important, as large variations in the total flow rate delivered to the gas sensors over the course of the experiment would cause a change in the sensor's resistances not attributable to a change in menthol vapor concentration.

II.D – Data Analysis with MATLAB

MATLAB was used to perform almost all of the data analysis and visualization required for this project.

Beginning in July 2019, a comprehensive MATLAB script with dozens of custom supporting functions was authored almost solely by me (but with input and ideas from others) to import, filter, analyze and visualize raw gas sensor data on a large scale. Additional features and functionalities have been gradually added to the script since then as different needs have arisen. The program was designed for the high throughput screening of gas sensors for research and development purposes. The only constraints on the amount of gas sensor data that could be processed at any one time were the amounts of local computer memory and storage space available. Individual sensors were assigned unique IDs, and the plots of raw gas sensor data and any quantities derived from them were labeled according to a user-supplied spreadsheet that associated

specific sensors with certain labels, such as a name for the sensor and the units associated with the raw sensor data.

The MATLAB script imported raw transient sensor data (e.g. resistance versus time), a spreadsheet which describes when the sensors where exposed to specific gas mixtures during the experiment, a spreadsheet which includes identifying labels for each sensor, and a few other user inputs which control how certain quantities were to be calculated and plots were to be generated. After receiving the necessary inputs, MATLAB processed the data and exports several files for each sensor such as raw data plots, a table summarizing different quantitative sensor response characteristics for each exposure step in the experiment and a calibration plot which showed how the magnitude of the sensor response correlated with the concentration of analyte.

In addition to the program described above (which is now in use by different members of the Myung group), a shorter supplemental MATLAB script was authored by me specifically for this capstone project. This script fit a line to the sensor response versus menthol concentration data, estimated the lower limit of detection (LLOD) and exported sensor response versus menthol concentration plots with and without linear fitting information displayed.

The MATLAB Curve Fitting Toolbox was used to fit the menthol vapor pressure versus temperature data from literature to obtain the Antoine equation.

The quantities calculated from the data analysis process are explained in section *III.B* with sample calculations.

III. Results and Discussion

III.A Menthol Antoine Equation

The menthol vapor pressure-temperature data that was collected from literature is plotted in **Figure 3**. Also plotted in this figure is the graph of the Antione equation that was determined to best fit the data. The best-fit Antoine equation for menthol was determined to be given by:

$$P_{vp,m}(T) = \exp\left(33.78 - \frac{9143}{T-13.9}\right) \quad (5)$$

In equation (5), $P_{vp,m}$ is the vapor pressure of menthol (Pa), T is the temperature (K) and *exp* denotes the exponential function ($\exp(x) = e^x$). Equation (1) fits the literature values of menthol vapor pressures over a range of temperatures from 273 K (25°C) to 315 K (42°C) with an $R^2 = 1.00$. This value of R^2 indicates that equation (1) fits the vapor pressure data almost perfectly, so it is suitable for calculating the vapor pressure and concentrations of menthol under the conditions encountered in the gas sensing experiments performed for this project.

The vapor pressure of menthol at 25°C (273 K) according to equation (5) is 0.221 Pa. Thus, per equation (3), the equilibrium concentration of vaporized menthol above a solid sample of menthol at a standard atmospheric pressure of 101325 Pa comes out to about 2.19 ppm. This is the maximum concentration of menthol vapor in air that could be generated in the experimental apparatus. Concentrations much lower than this were obtained by serial dilution as described in section *II.B*.

III.B – Sample Calculations of Sensor Responses and Characteristics

Except for the FCM 2630 (S000000004), which provided voltage data, all of the sensors that were exposed to menthol in the experiment provided raw data as measured resistances of the metal oxide sensing material in ohms. For the representative calculations explained below, the data from sensor S000000020 (MICS 6814 reducing channel) was used. **Figure 5** shows the raw

resistance data collected from this sensor during exposure to menthol, and **Figure 23** shows the computed normalized responses of this sensor as a function of menthol concentration.

Due to variations in the resistances between different sensors, even replicate sensors of the same type, it was necessary to normalize the gas sensor data by dividing all of the measured resistances by a "baseline" resistance. The baseline resistance for each sensor was taken to be the measured resistance of the sensors immediately before the first exposure to menthol, or, in other words, the measured resistance at the end of the initial 36 hour purging with air.

For example, the equilibrium resistance of S000000020 during its second exposure to 0.24 ppm of menthol was measured to be 4926 Ω. The baseline resistance of the sensor, or its equilibrium resistance immediately before the introduction of menthol vapor, was determined to be 4310 Ω. Thus, the normalized response of the sensor to this concentration of menthol was calculated to be:

$$\frac{R_s}{R_0} = \frac{4926\ \Omega}{4310\ \Omega} = 1.143$$

R_s is the resistance of sensor during exposure to menthol and R_0 is the baseline resistance in the absence of menthol. Three responses from each menthol concentration were obtained and averaged together to give the responses shown in **Figure 23**. The error bars in that figure represent three standard deviations, or a signal-to-noise ratio of three, which is regarded as an acceptable statistical cutoff for reporting and distinguishing between sensor responses.[9]

Although the response of metal oxide sensors as a function of analyte concentration is typically nonlinear,[2] it may be approximately linear over a limited concentration range. It was found that a line could be used to accurately fit the normalized responses of some of the sensors ($R^2 > 0.98$) over a narrow range of menthol concentrations as shown in **Figures 23** through **32**.

$$\frac{R_S}{R_0} = aC + b \quad (6)$$

In equation (6), a is the normalized linear sensitivity (ppm^{-1}), C is the menthol concentration (ppm) and b is the y-intercept (dimensionless). A positive value of a indicated that a sensor had an increase in resistance when exposed to menthol, while a negative value indicated a decrease. For S000000020, it was found that $a = 0.7032$ and $b = 0.9641$ (**Figure 23**).

The LLOD is the minimum concentration of menthol expected to produce an observable change in sensor resistance. Equation (6) was used to estimate the LLOD, or lower limit of detection, of menthol for the sensors which showed a response. This was done by setting equation (6) equal to one and solving for C:

$$C_{LLOD} = \frac{1-b}{a} \quad (7)$$

From equation (7), the extrapolated menthol LLOD for sensor S000000020 was calculated to be 0.051 ppm. All of these values for sensor S000000020 were reported in **Table 3**.

III.C – Summary and Discussion of Sensor Response Characteristics

Table 3 summarizes the response characteristics of the evaluated gas sensors towards menthol vapor. It lists the qualitative response towards menthol, normalized linear sensitivity, extrapolated menthol LLOD and linear response concentration range. Sensors with very weak or no response to menthol were not subjected to further analysis as described in the previous subsection. Entries in the table for which values could not be calculated due to a lack of a clear response of the sensor towards menthol vapor were labeled "NC".

The MICS 6814 units each contained three sensors: reducing, oxidizing and NH3. Data was obtained for two MICS 6814 units (S000000020 through S000000025), but only the reducing and NH3 channels on one of the units (S000000020, S000000022) strongly responded to menthol vapor with an increase in resistance, while the oxidizing channel (S000000021) responded very

weakly and noisily. The MICS 6814 reducing and NH3 sensors were the only sensors that displayed an increase in resistance upon exposure to menthol; all the other sensors displayed decreases in resistance. The MICS 6814 NH3 channel (S000000022) also displayed the highest normalized linear sensitivity among all of the gas sensors that were evaluated in this project at 0.964 ppm^{-1}.

One of the BME 680 sensors (S000000036) showed a clear decrease in resistance when exposed to menthol vapor (**Figures 17** and **31**), while a second BME 680 (S000000037) showed no response towards menthol whatsoever (**Figure 18**).

Both MICS 4514 units (S000000028 through S000000031), each with reducing and oxidizing channels, showed strong responses to menthol vapor as can be seen in **Figures 13** through **16** and **27** through **30**. For both sensors, the reducing channels had a higher linear sensitivity than the oxidizing channels.

Both MICS 5524 units (S000000026 and S000000027) showed clear and comparable resistance decreases when exposed to menthol vapor (**Figures 11**, **12**, **25** and **26**). One of the MICS 5524 reducing sensors had the lowest extrapolated menthol LLOD at 0.014 ppm.

The TGS 2603 (S000000038) showed a clear resistance decrease when exposed to menthol vapor (**Figures 19** and **32**).

The FCM 2630 (S000000004, **Figure 4**), TGS 832-A00 (S000000040 and S000000041, **Figures 20** and **21**) and TGS 3830 (S000000040, **Figure 22**) did not show clear responses to menthol vapor at the concentrations evaluated in this project.

From the results that were obtained, it was clear that menthol vapor can be detected and quantified by some of the metal oxide gas sensors in the hundreds of parts per billion, possibly down to tens of parts per billion if the extrapolated LLODs are accurate.

It is possible that the replicate MICS 6814 and BME 680 units, plus any of the other sensors which did not show a response to menthol vapor, were wired incorrectly, had been poisoned by an outside contaminant or had simply been used beyond their useful lifespan. Degradation of the response characteristics of metal oxide gas sensors over time as a result of the functional metal oxide particles sintering at the high operating temperatures and other factors is a well-known issue and a key weakness of metal oxide-based gas sensors.[10]

Both a high sensitivity and low LLOD are desired for gas sensors in many different applications. Of all of the sensors evaluated which responded to menthol, S000000022 (MICS 6814 NH3 Channel) had the highest magnitude of linear sensitivity observed at 0.964 ppm^{-1}, while S000000027 (MICS 5524) had the lowest extrapolated LLOD observed at 0.014 ppm. In the context of the Interstitial Cystitis diagnostics, a low LLOD for menthol vapor is an especially desirable response characteristic.

IV. Future Work and Research Directions

Although the menthol gas sensing results described above are promising for detecting and quantifying menthol vapor in the headspace above a urine sample and show that it is certainly feasible, these measurements were taken under highly controlled conditions in the absence of other contaminants. In the urine vapor headspace, water vapor and other volatile compounds present in urine would undoubtedly interfere with attempts to directly quantify the amount of menthol present in the sample. Many metal oxide-based gas sensors lack *selectivity*, which means that many different compounds can react with the absorbed oxides on the metal oxide surface to produce an observable change in resistance.

There are several possible approaches to overcome these issues to improve sensor selectivity. I explored some possibilities from a materials engineering perspective in a review article that I recently co-authored and published with other members of the Myung group titled *Nanoengineering Approaches Toward Artificial Nose*.[11]

One possibility is to engineer and attach an organic ligand, or molecule, to the surface of the active semiconducting material. The organic ligand would be structured in such a way that it would bind preferentially with menthol molecules so that only they would cause the conductivity (or other properties) of the semiconducting material to change irrespective of whatever else is present. Of course, this is much easier said than actually done, and it may not even be possible (but it might be worth exploring!).

Another possible approach is to bypass the difficult problem of directly quantifying menthol in the complex urine vapor headspace entirely. The use of an array of cross-sensitive gas sensors to make an *electronic nose* may be sufficient if merely classifying urine samples as healthy or not is the end goal. Machine learning and deep learning computational methods may be used to interpret data from several gas sensors to classify a urine sample as either belonging or not belonging to someone who has interstitial cystitis based on subtle differences in how the different sensors respond to both types of urine samples. It may also be possible to quantify menthol vapor concentration or the concentration of menthol dissolved in the urine using regression models.

V. Figures and Figure Captions

Figure 1: Chemical structure of (*l*)-menthol

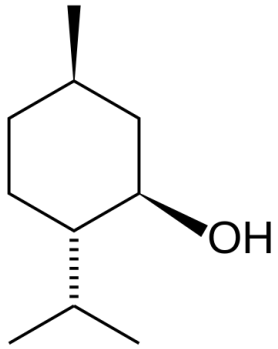

Figure 1: This figure depicts the chemical structure of the naturally occurring (*l*)-menthol enantiomer.

Figure 2: Diagram of Vapor-generation Apparatus

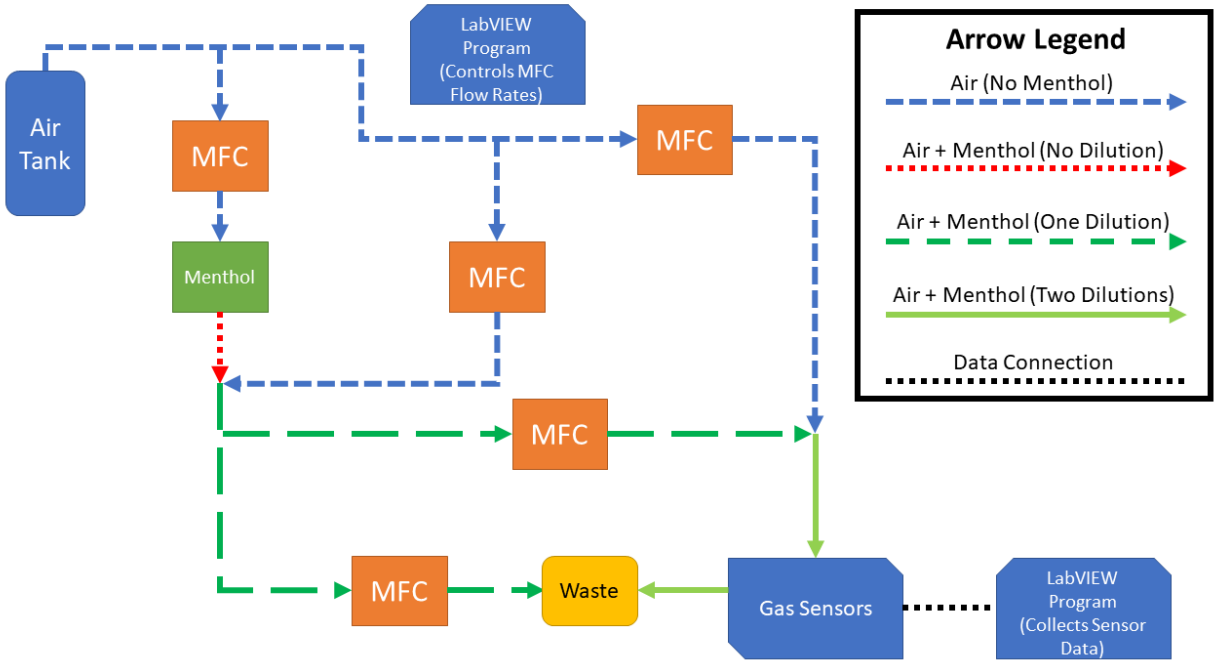

Figure 2: This figure outlines the structure of the custom apparatus that was used to continuously generate mixtures of air and menthol with a known, dilute menthol concentration. The arrows

indicate the direction of gas flow, and the style of the lines indicate the level of dilution according to the legend. The data connections between the LabVIEW program which controls the MFC flow rates and the MFCs are omitted for the sake of clarity.

Figure 3: (*l*)-menthol Vapor Pressure and Antoine Equation

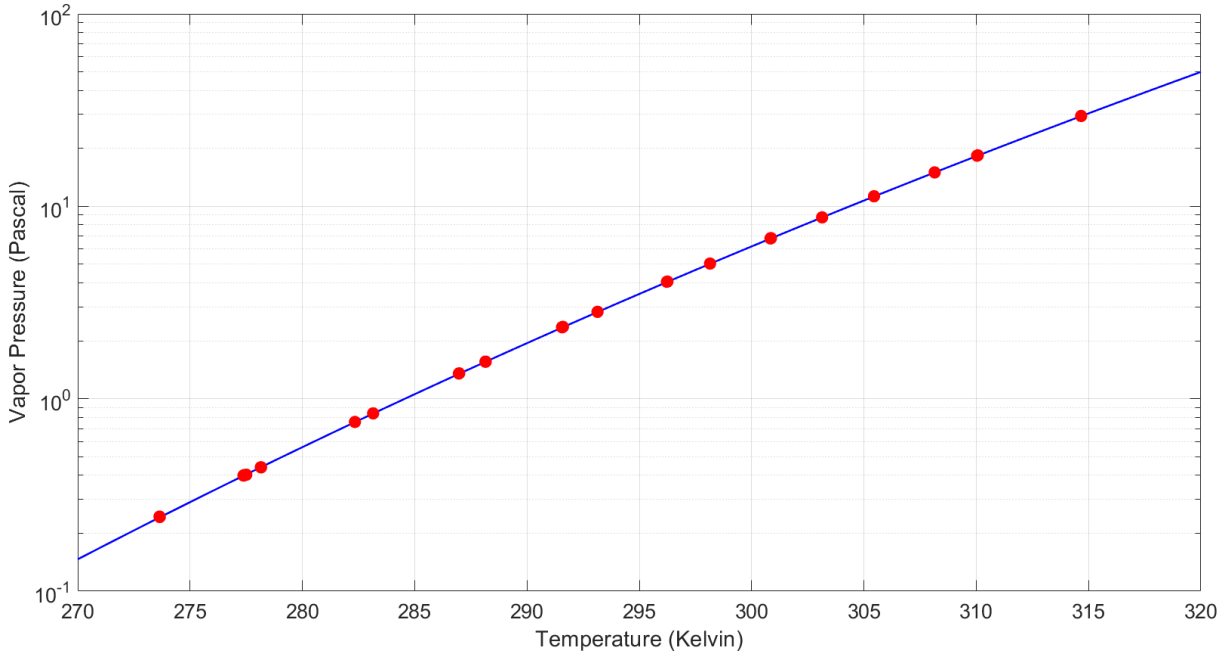

Figure 3: This figure shows the literature data for (*l*)-menthol vapor pressure (Pa) versus temperature (K) as individual data points (red).[7] The solid curve (blue) is a three-parameter Antoine equation that best fits the data. The Antoine equation is given in equation (5).

Figure 4: Raw Response of Sensor S000000004 (FCM 2630) to Menthol

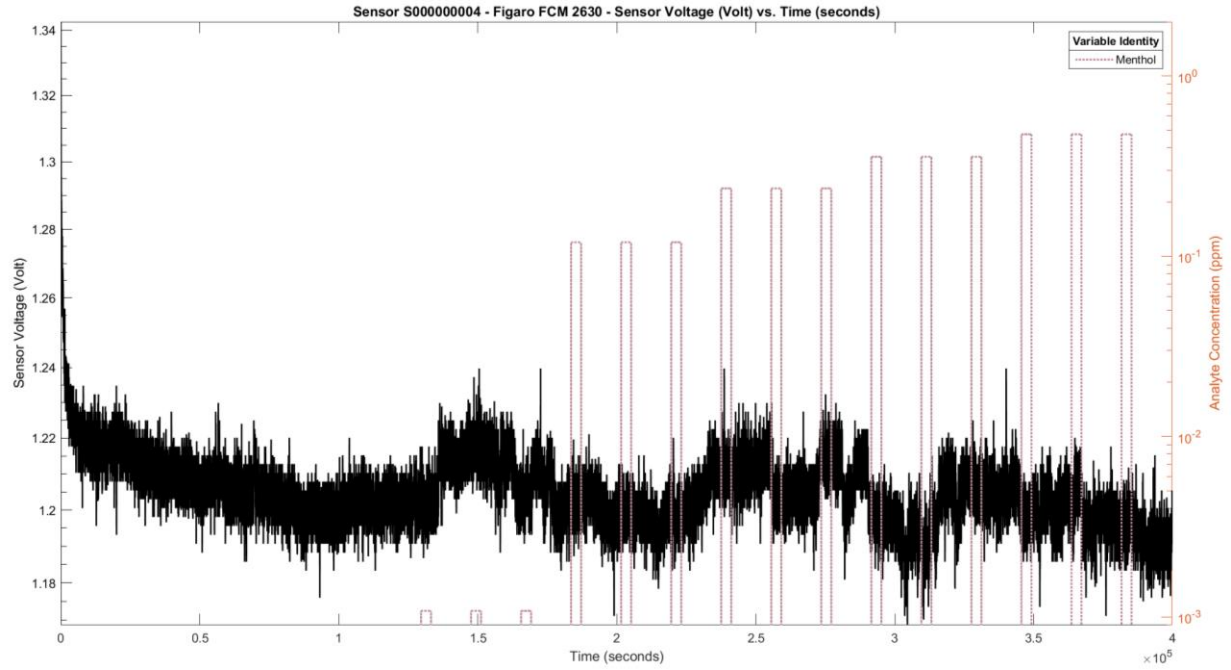

Figure 4: This figure shows the raw voltage measurements of the FCM 2630 taken during menthol exposure. The boundaries of the y-axis have been rescaled to show the response (if any) of the sensor towards menthol more clearly.

Figure 5: Raw Response of Sensor S000000020 (MICS 6814 Reducing Channel) to Menthol

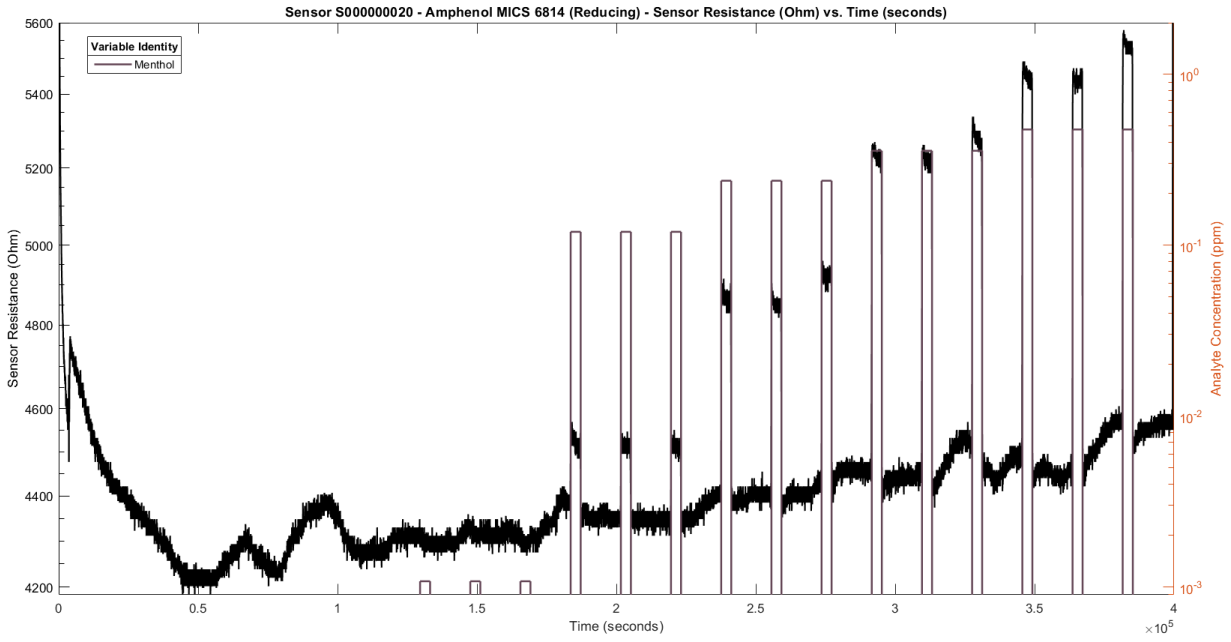

Figure 5: This figure shows the raw resistance measurements of the MICS 6814 Reducing Channel taken during menthol exposure. The boundaries of the y-axis have been rescaled to show the response (if any) of the sensor towards menthol more clearly.

Figure 6: Raw Response of Sensor S000000021 (MICS 6814 Oxidizing Channel) to Menthol

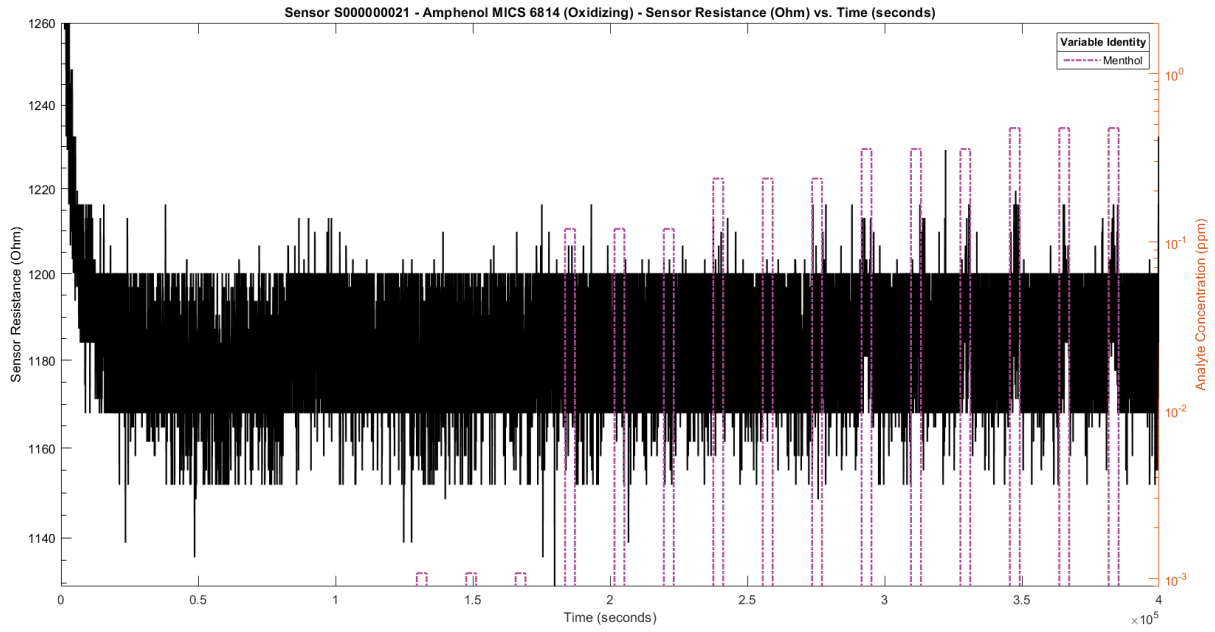

Figure 6: This figure shows the raw resistance measurements of the MICS 6814 Oxidizing Channel taken during menthol exposure. The boundaries of the y-axis have been rescaled to show the response (if any) of the sensor towards menthol more clearly.

Figure 7: Raw Response of Sensor S000000022 (MICS 6814 NH3 Channel) to Menthol

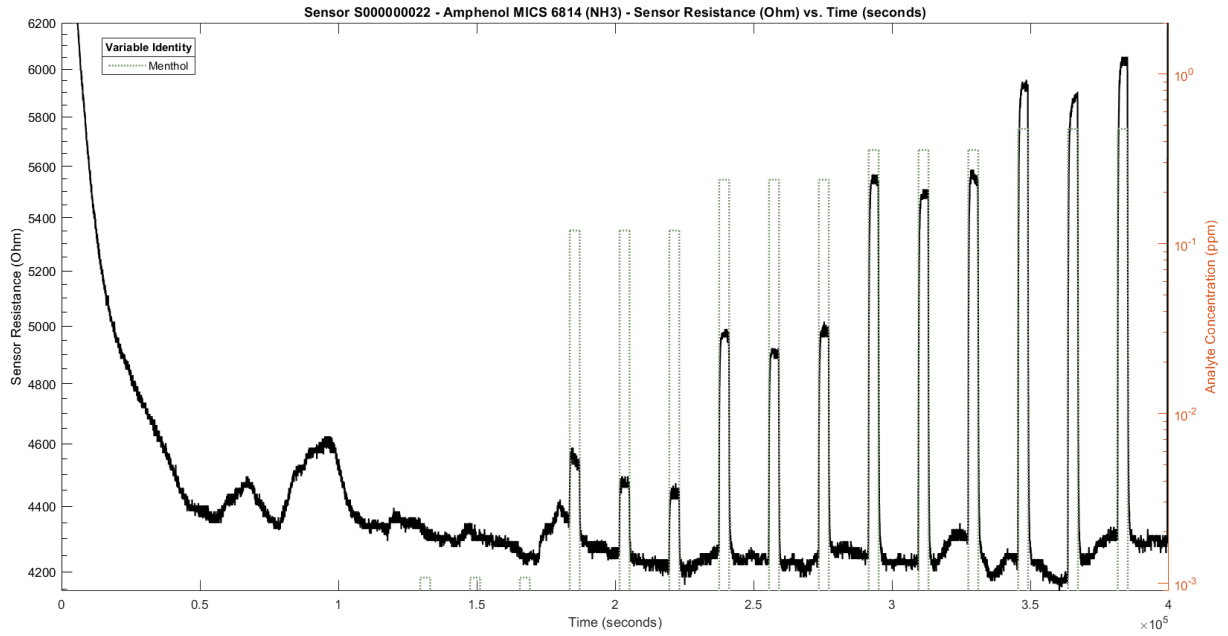

Figure 7: This figure shows the raw resistance measurements of the MICS 6814 NH3 Channel taken during menthol exposure. The boundaries of the y-axis have been rescaled to show the response (if any) of the sensor towards menthol more clearly.

Figure 8: Raw Response of Sensor S000000023 (MICS 6814 Reducing Channel) to Menthol

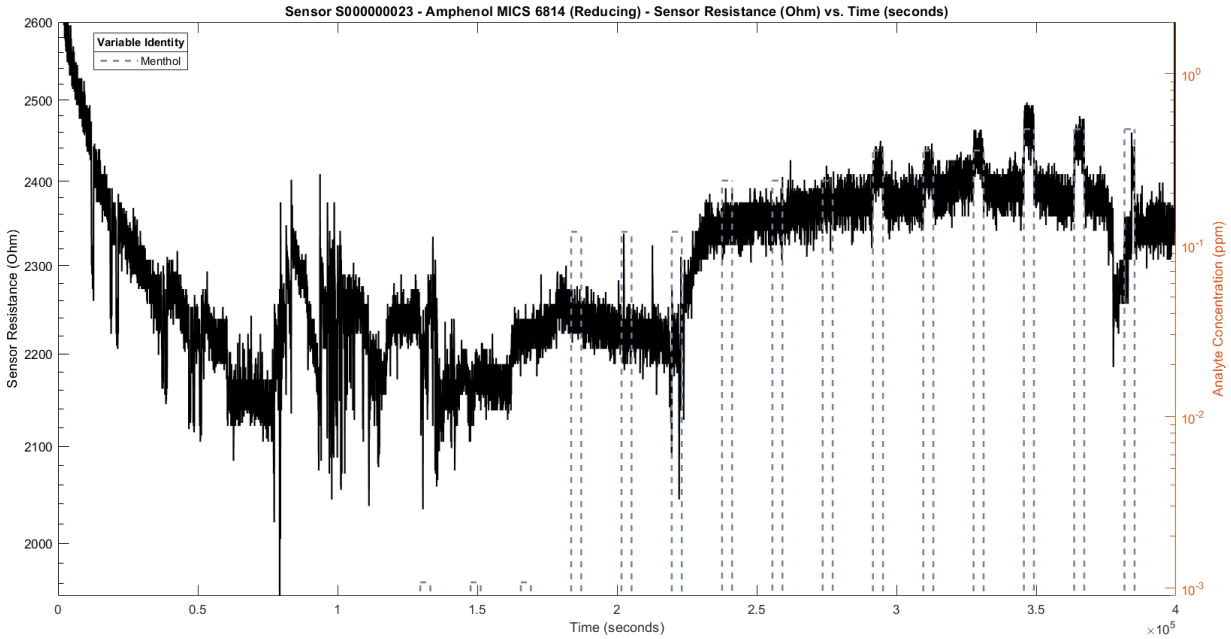

Figure 8: This figure shows the raw resistance measurements of the MICS 6814 Reducing Channel taken during menthol exposure. The boundaries of the y-axis have been rescaled to show the response (if any) of the sensor towards menthol more clearly.

Figure 9: Raw Response of Sensor S000000024 (MICS 6814 Oxidizing Channel) to Menthol

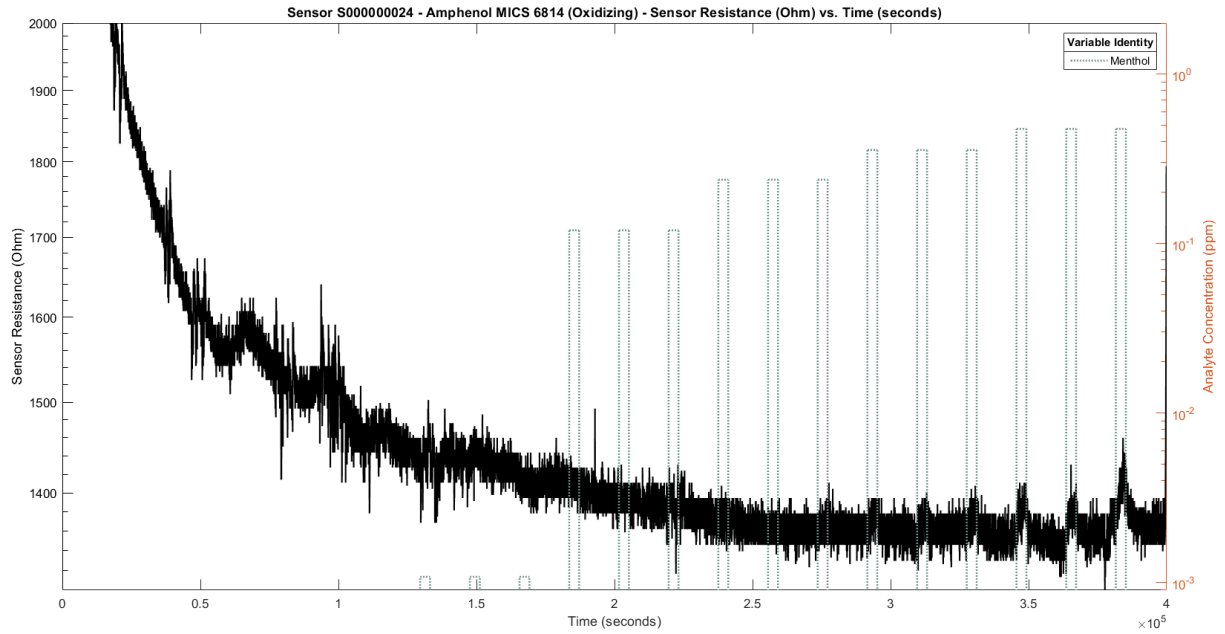

Figure 9: This figure shows the raw resistance measurements of the MICS 6814 Oxidizing Channel taken during menthol exposure. The boundaries of the y-axis have been rescaled to show the response (if any) of the sensor towards menthol more clearly.

Figure 10: Raw Response of Sensor S000000025 (MICS 6814 NH3 Channel) to Menthol

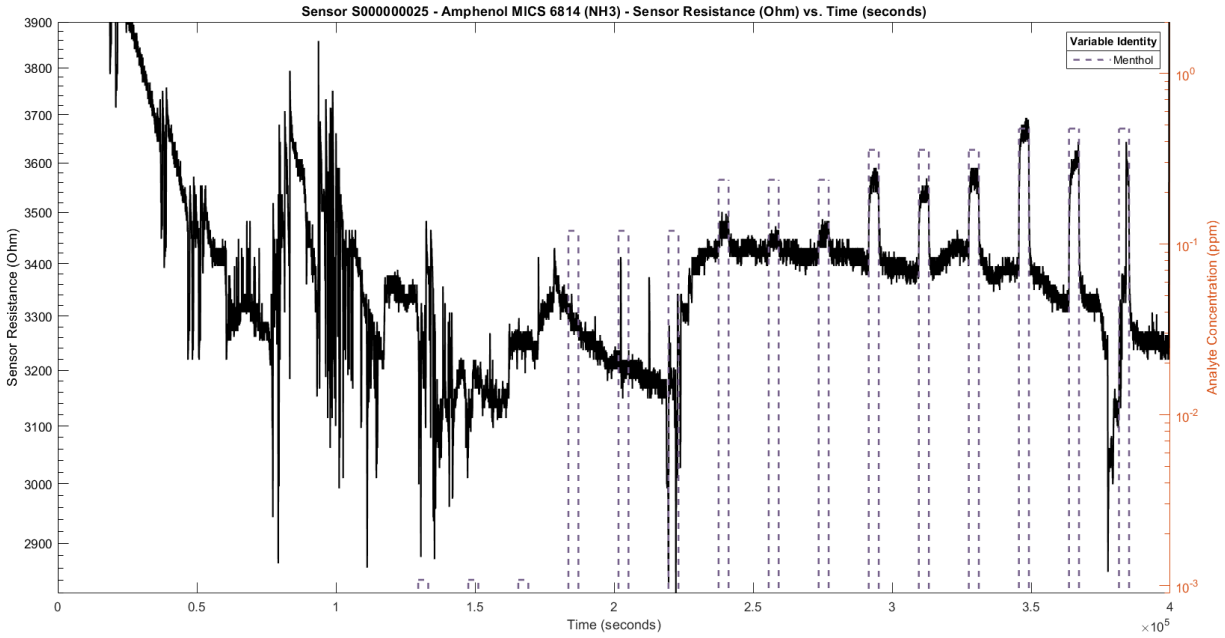

Figure 10: This figure shows the raw resistance measurements of the MICS 6814 NH3 Channel taken during menthol exposure. The boundaries of the y-axis have been rescaled to show the response (if any) of the sensor towards menthol more clearly.

Figure 11: Raw Response of Sensor S000000026 (MICS 5524) to Menthol

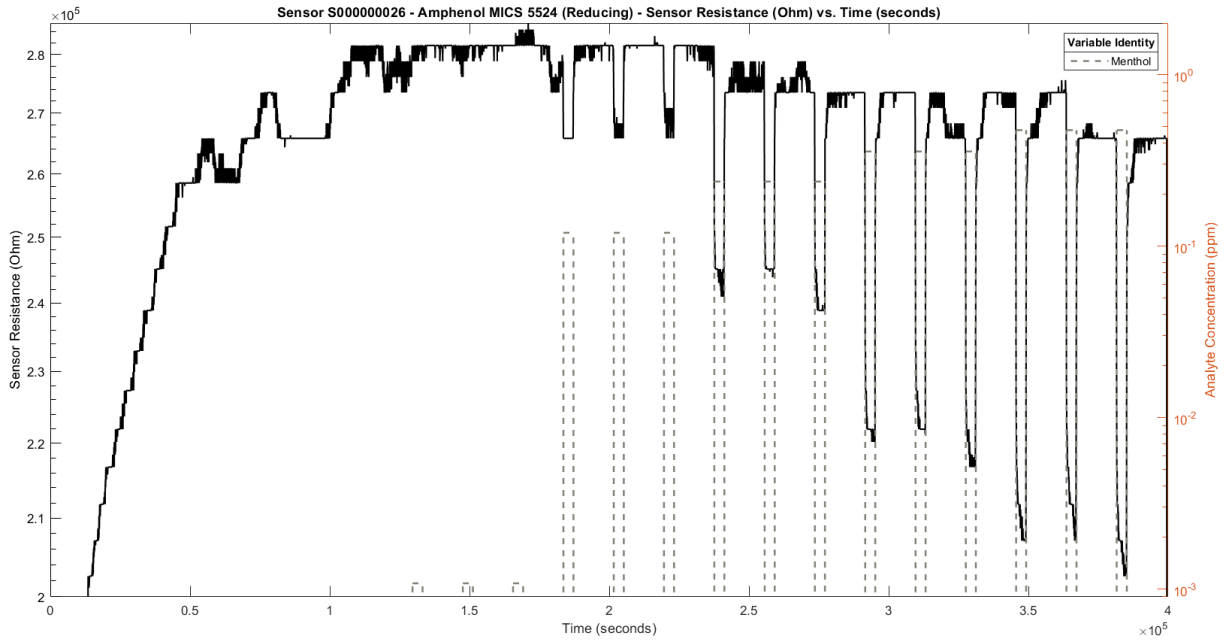

Figure 11: This figure shows the raw resistance measurements of the MICS 5524 taken during menthol exposure. The boundaries of the y-axis have been rescaled to show the response (if any) of the sensor towards menthol more clearly.

Figure 12: Raw Response of Sensor S000000027 (MICS 5524) to Menthol

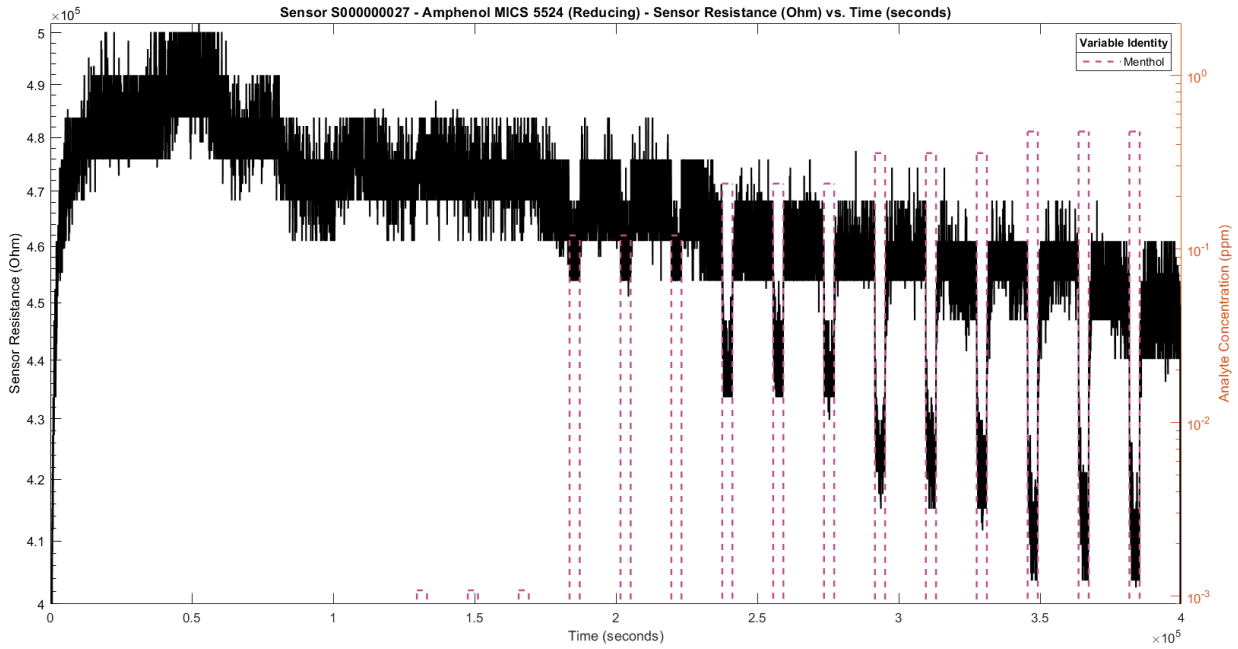

Figure 12: This figure shows the raw resistance measurements of the MICS 5524 taken during menthol exposure. The boundaries of the y-axis have been rescaled to show the response (if any) of the sensor towards menthol more clearly.

Figure 13: Raw Response of Sensor S000000028 (MICS 4514 Reducing Channel) to Menthol

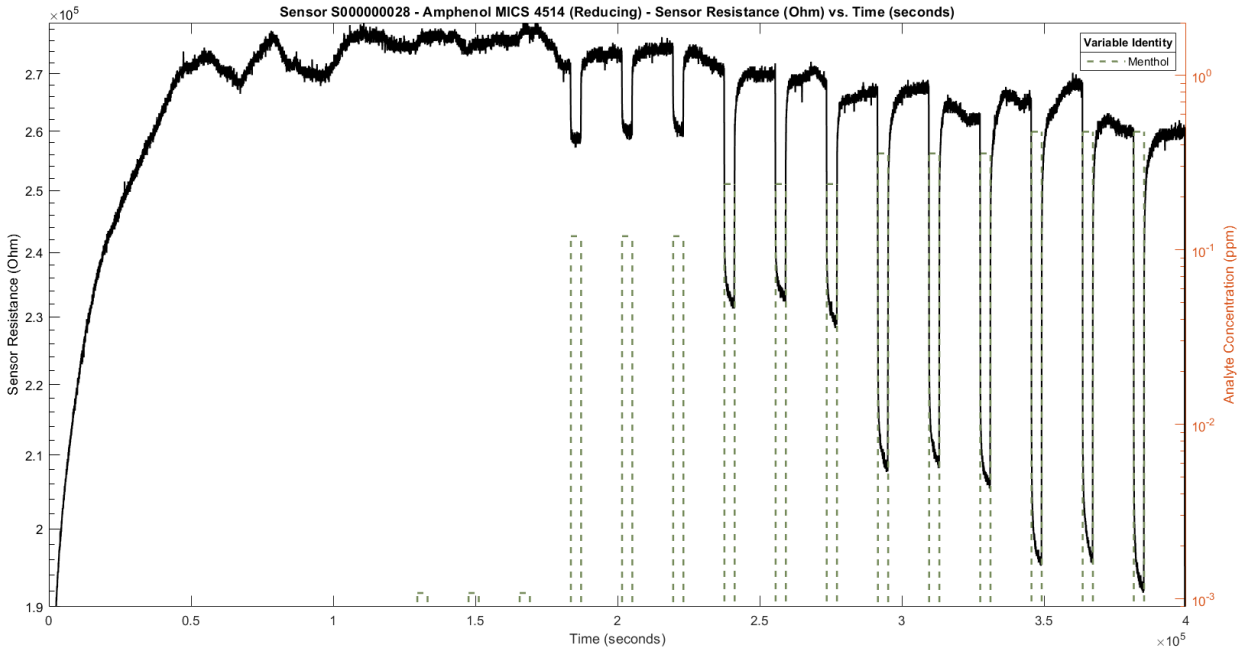

Figure 13: This figure shows the raw resistance measurements of the MICS 4514 Reducing Channel taken during menthol exposure. The boundaries of the y-axis have been rescaled to show the response (if any) of the sensor towards menthol more clearly.

Figure 14: Raw Response of Sensor S000000029 (MICS 4514 Oxidizing Channel) to Menthol

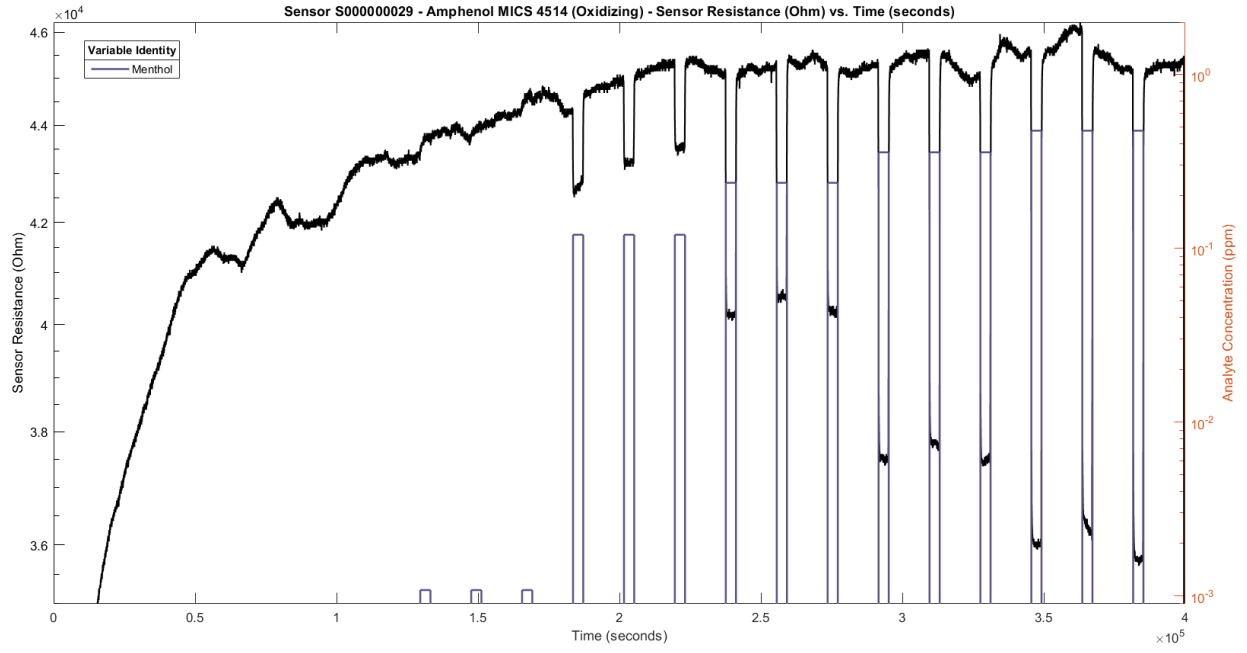

Figure 14: This figure shows the raw resistance measurements of the MICS 4514 Oxidizing Channel taken during menthol exposure. The boundaries of the y-axis have been rescaled to show the response (if any) of the sensor towards menthol more clearly.

Figure 15: Raw Response of Sensor S000000030 (MICS 4514 Reducing Channel) to Menthol

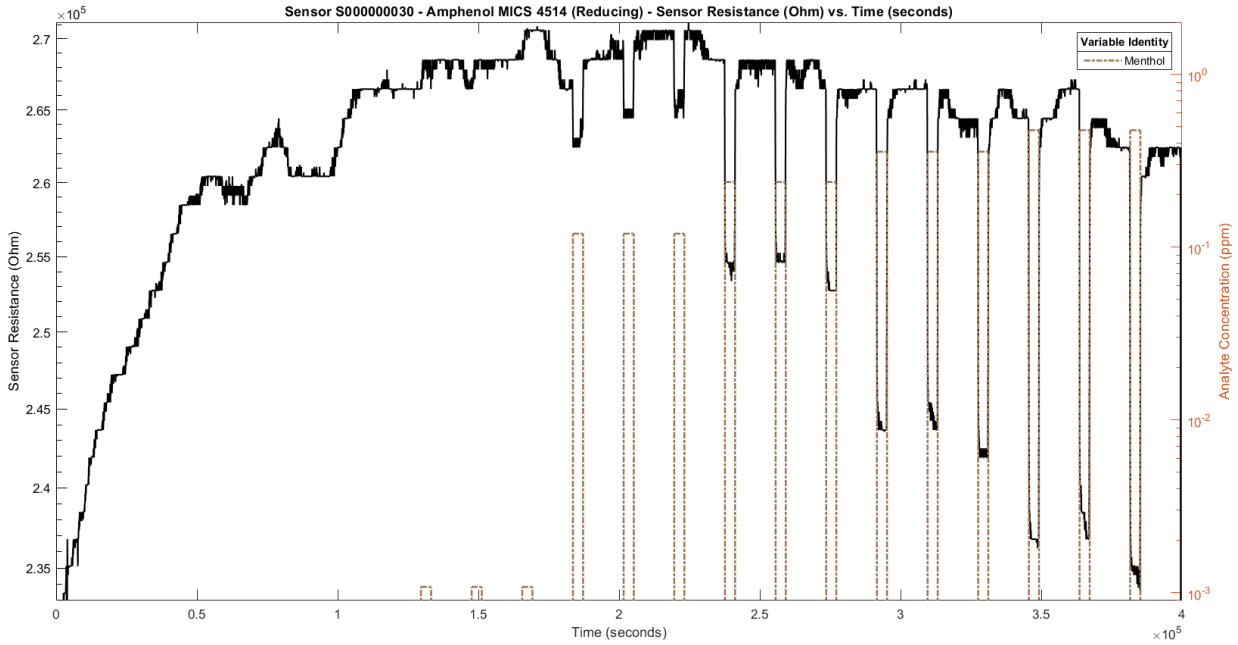

Figure 15: This figure shows the raw resistance measurements of the MICS 4514 Reducing Channel taken during menthol exposure. The boundaries of the y-axis have been rescaled to show the response (if any) of the sensor towards menthol more clearly.

Figure 16: Raw Response of Sensor S000000031 (MICS 4514 Oxidizing Channel) to Menthol

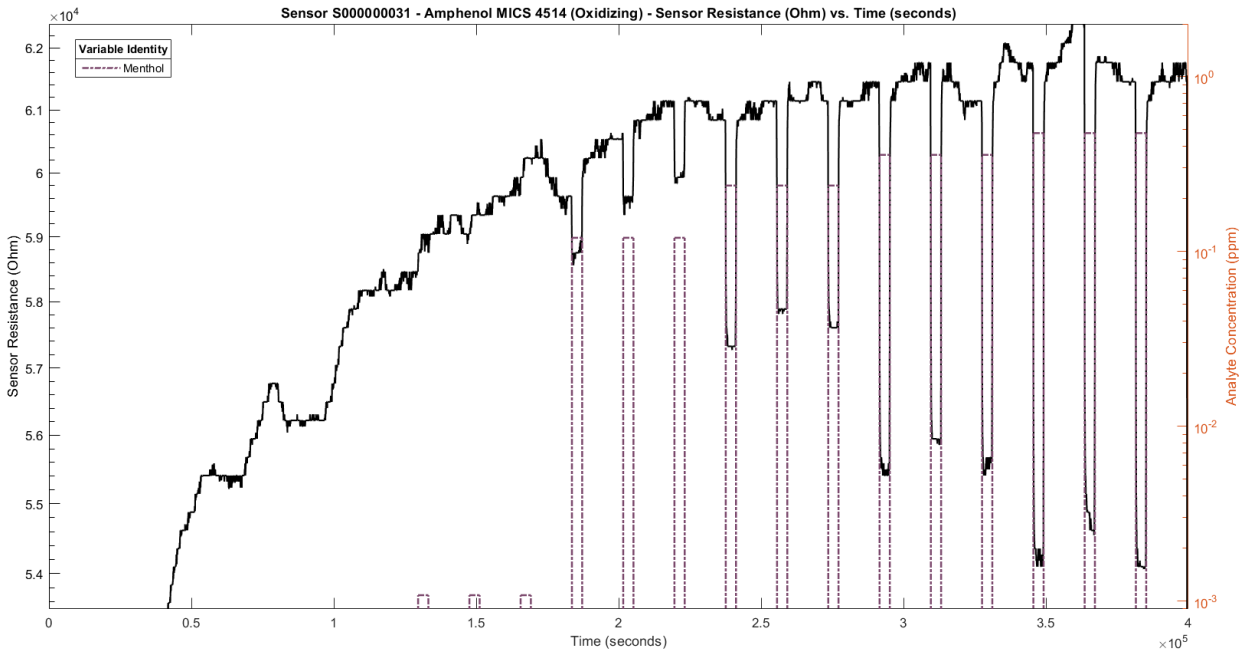

Figure 16: This figure shows the raw resistance measurements of the MICS 4514 Oxidizing Channel taken during menthol exposure. The boundaries of the y-axis have been rescaled to show the response (if any) of the sensor towards menthol more clearly.

Figure 17: Raw Response of Sensor S000000036 (BME 680) to Menthol

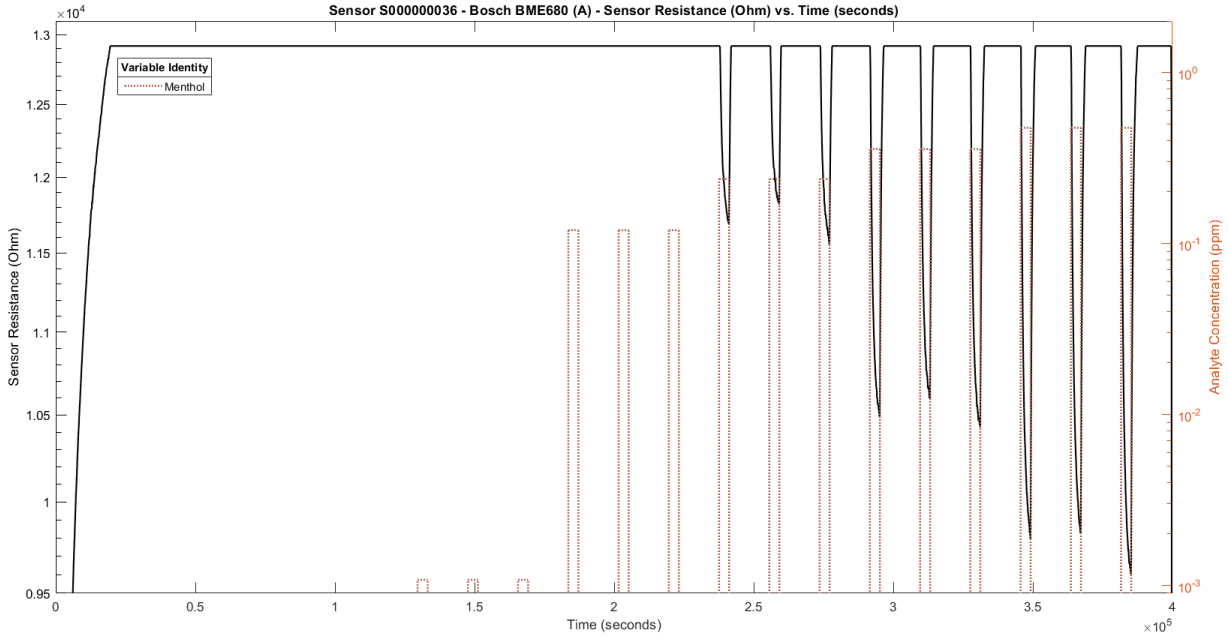

Figure 17: This figure shows the raw resistance measurements of the BME 680 taken during menthol exposure. The boundaries of the y-axis have been rescaled to show the response (if any) of the sensor towards menthol more clearly.

Figure 18: Raw Response of Sensor S000000037 (BME 680) to Menthol

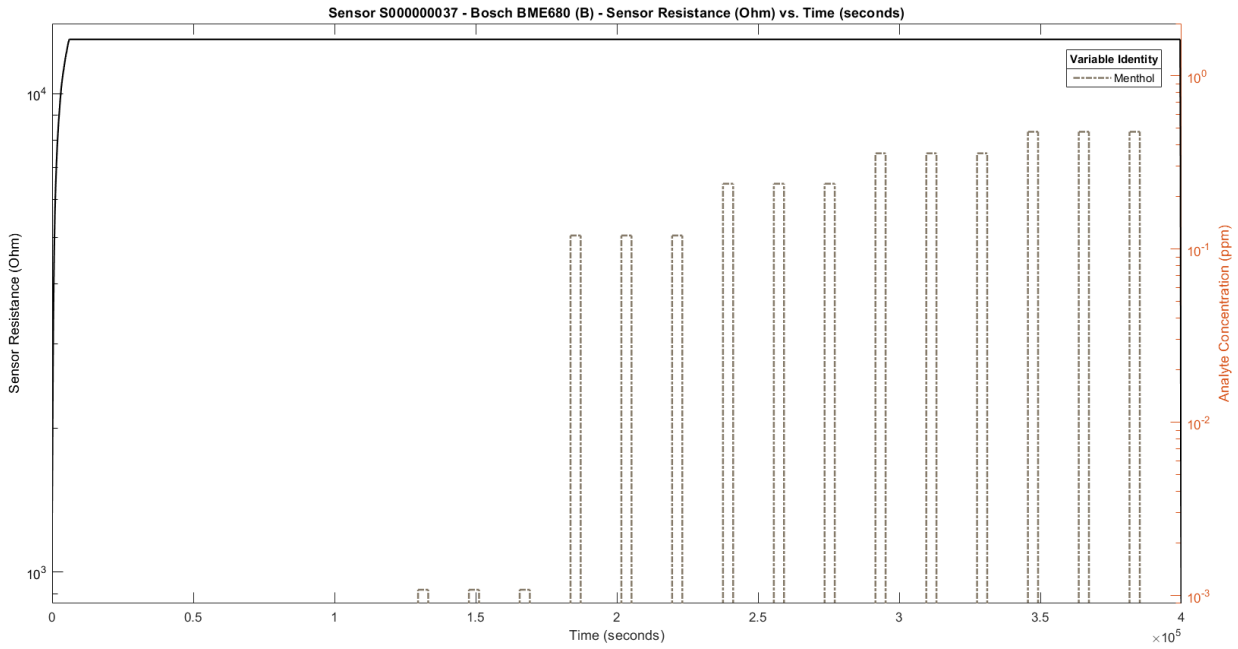

Figure 18: This figure shows the raw resistance measurements of the BME 680 taken during menthol exposure. The boundaries of the y-axis have been rescaled to show the response (if any) of the sensor towards menthol more clearly.

Figure 19: Raw Response of Sensor S000000038 (TGS 2603) to Menthol

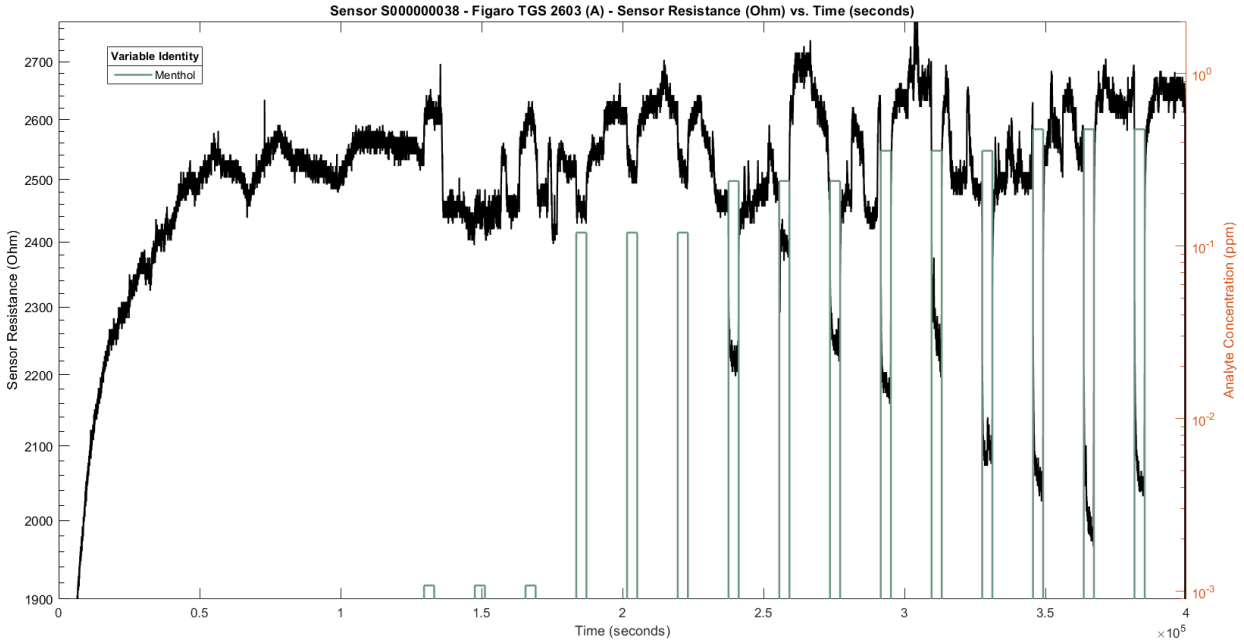

Figure 19: This figure shows the raw resistance measurements of the TGS 2603 taken during menthol exposure. The boundaries of the y-axis have been rescaled to show the response (if any) of the sensor towards menthol more clearly.

Figure 20: Raw Response of Sensor S000000040 (TGS 832-A00) to Menthol

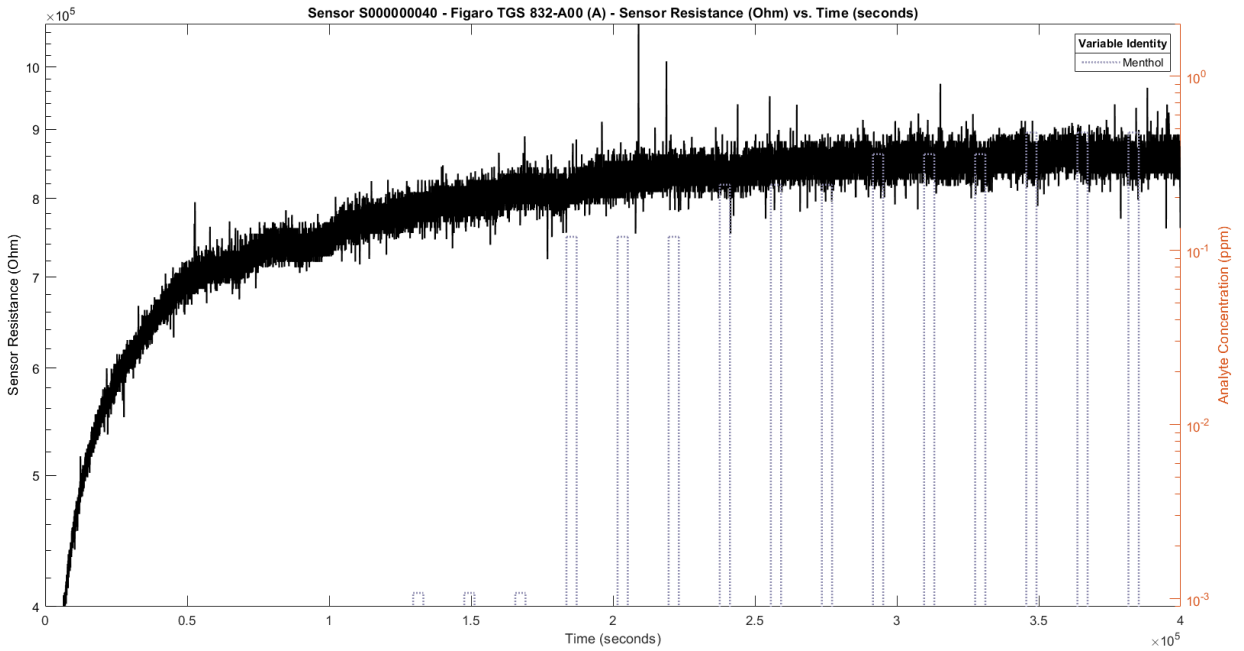

Figure 20: This figure shows the raw resistance measurements of the TGS 832-A00 taken during menthol exposure. The boundaries of the y-axis have been rescaled to show the response (if any) of the sensor towards menthol more clearly.

Figure 21: Raw Response of Sensor S000000041 (TGS 832-A00) to Menthol

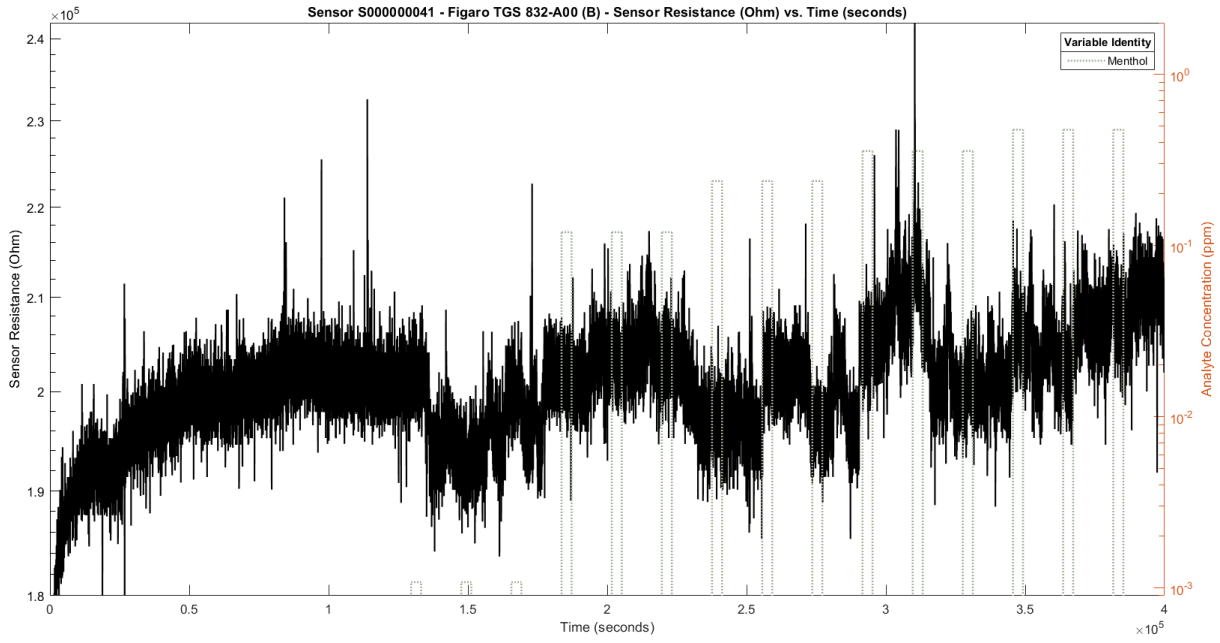

Figure 21: This figure shows the raw resistance measurements of the TGS 832-A00 taken during menthol exposure. The boundaries of the y-axis have been rescaled to show the response (if any) of the sensor towards menthol more clearly.

Figure 22: Raw Response of Sensor S000000044 (TGS 3830) to Menthol

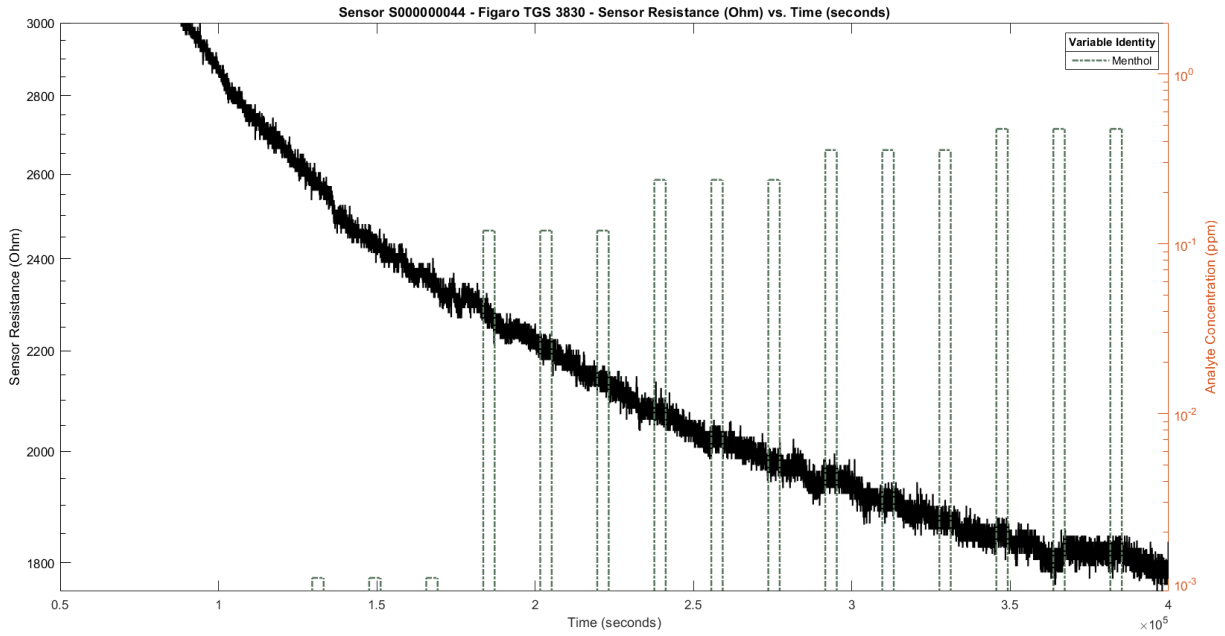

Figure 22: This figure shows the raw resistance measurements of the TGS 3830 taken during menthol exposure. The boundaries of the y-axis have been rescaled to show the response (if any) of the sensor towards menthol more clearly.

Figure 23: Calibration Plot of Sensor S000000020 (MICS 6184 Reducing Channel)

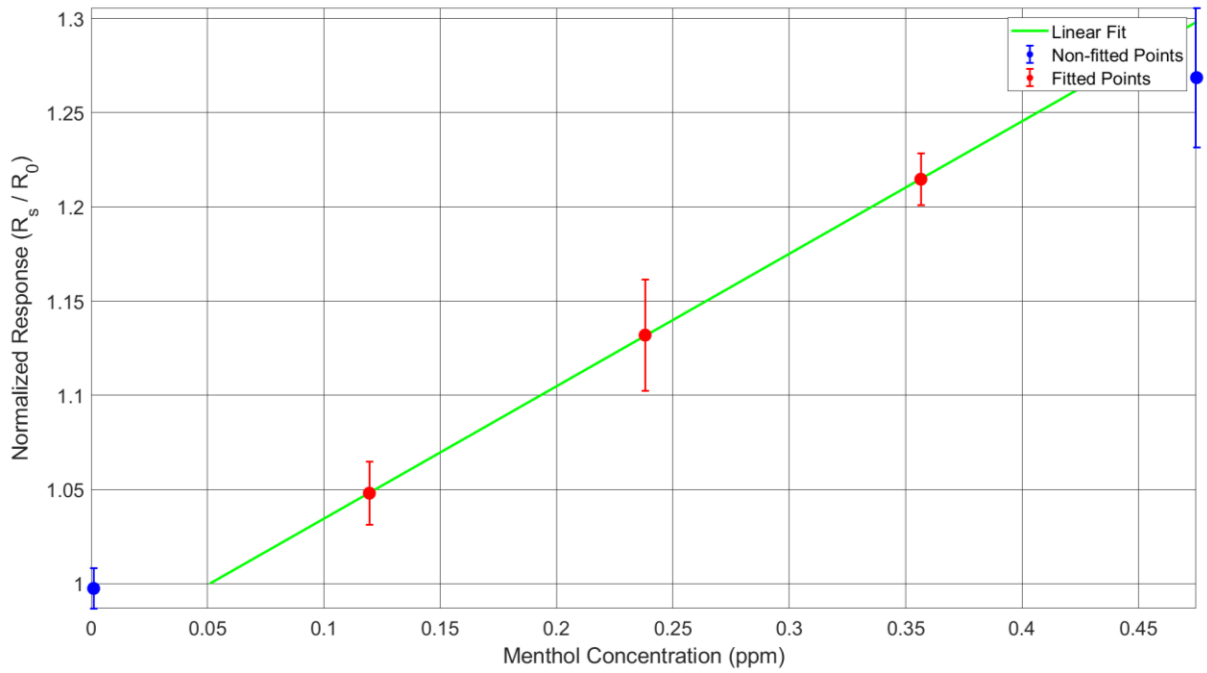

Figure 23: This figure shows the normalized response of the MICS 6814 Reducing Channel as a function of menthol concentration in ppm. The green line is the best-fit line of the linear response region given by the red points. The error bars indicate the range of three standard deviations in the observed response.

Figure 24: Calibration Plot of Sensor S000000022 (MICS 6184 NH3 Channel)

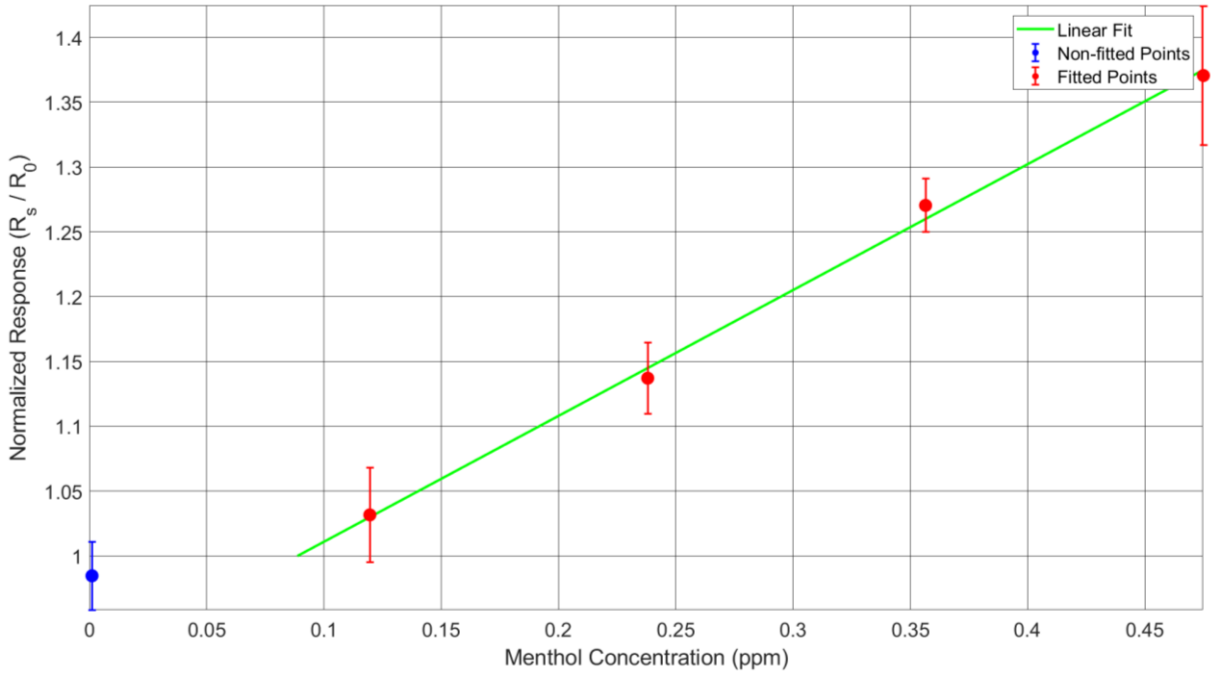

Figure 24: This figure shows the normalized response of the MICS 6814 NH3 Channel as a function of menthol concentration in ppm. The green line is the best-fit line of the linear response region given by the red points. The error bars indicate the range of three standard deviations in the observed response.

Figure 25: Calibration Plot of Sensor S000000026 (MICS 5524)

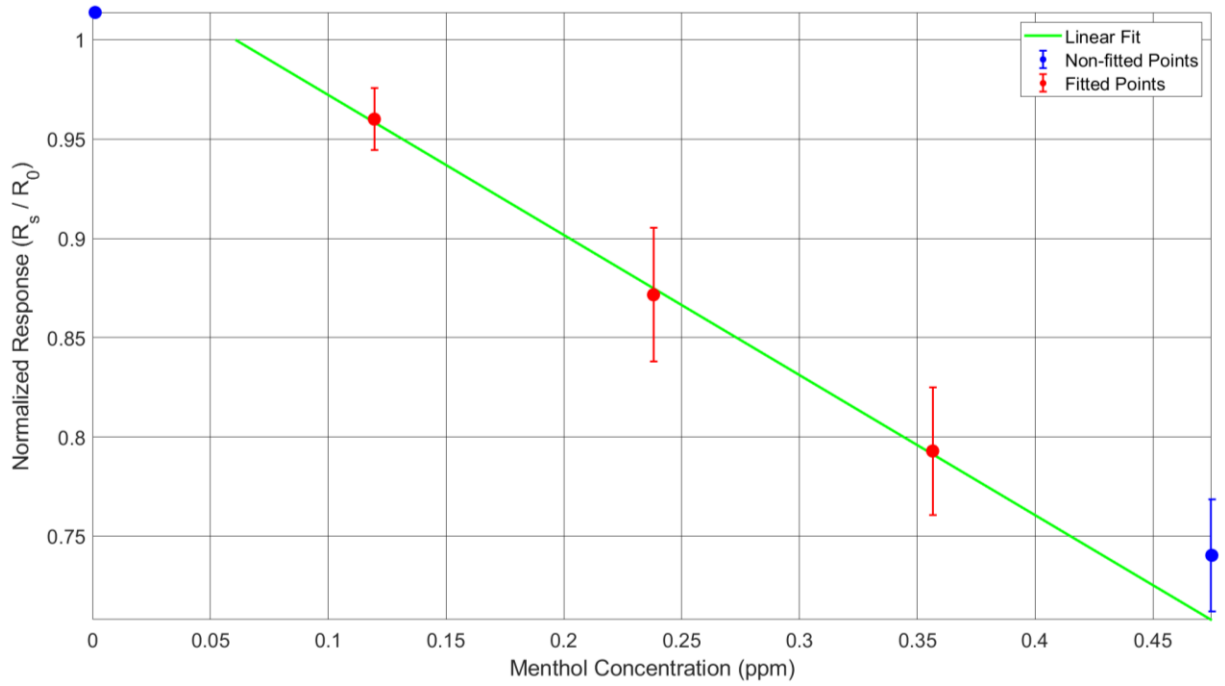

Figure 25: This figure shows the normalized response of the MICS 5524 as a function of menthol concentration in ppm. The green line is the best-fit line of the linear response region given by the red points. The error bars indicate the range of three standard deviations in the observed response.

Figure 26: Calibration Plot of Sensor S000000027 (MICS 5524)

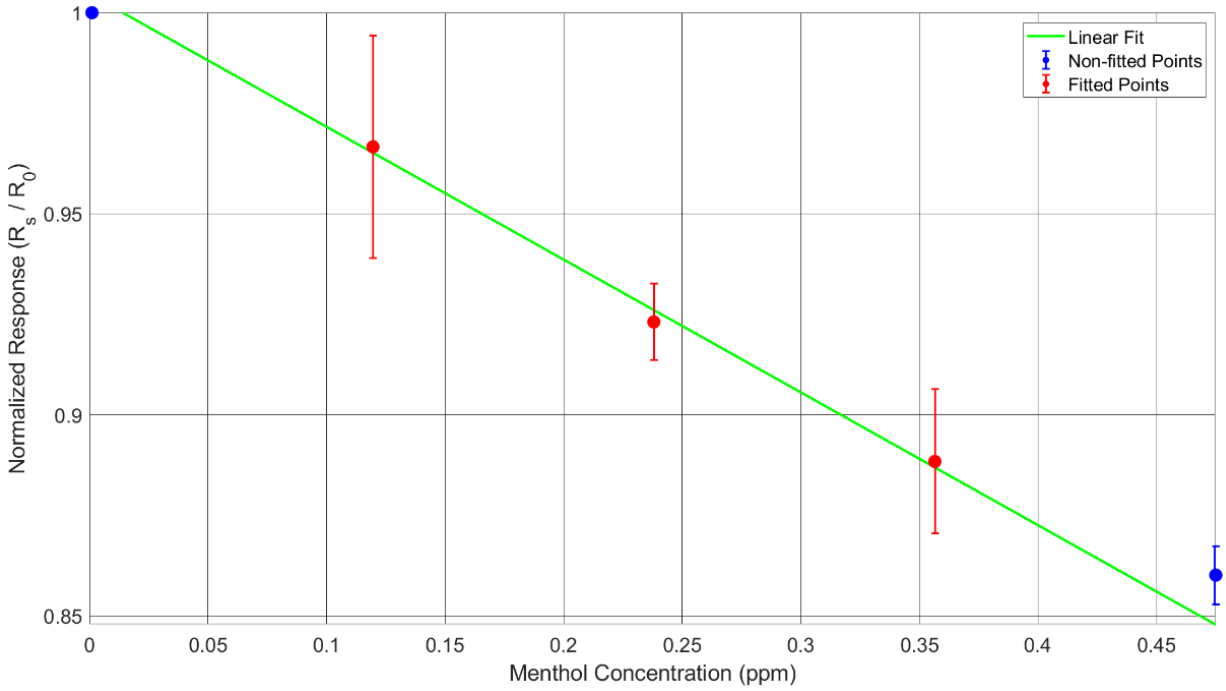

Figure 26: This figure shows the normalized response of the MICS 5524 as a function of menthol concentration in ppm. The green line is the best-fit line of the linear response region given by the red points. The error bars indicate the range of three standard deviations in the observed response.

Figure 27: Calibration Plot of Sensor S000000028 (MICS 4514 Reducing Channel)

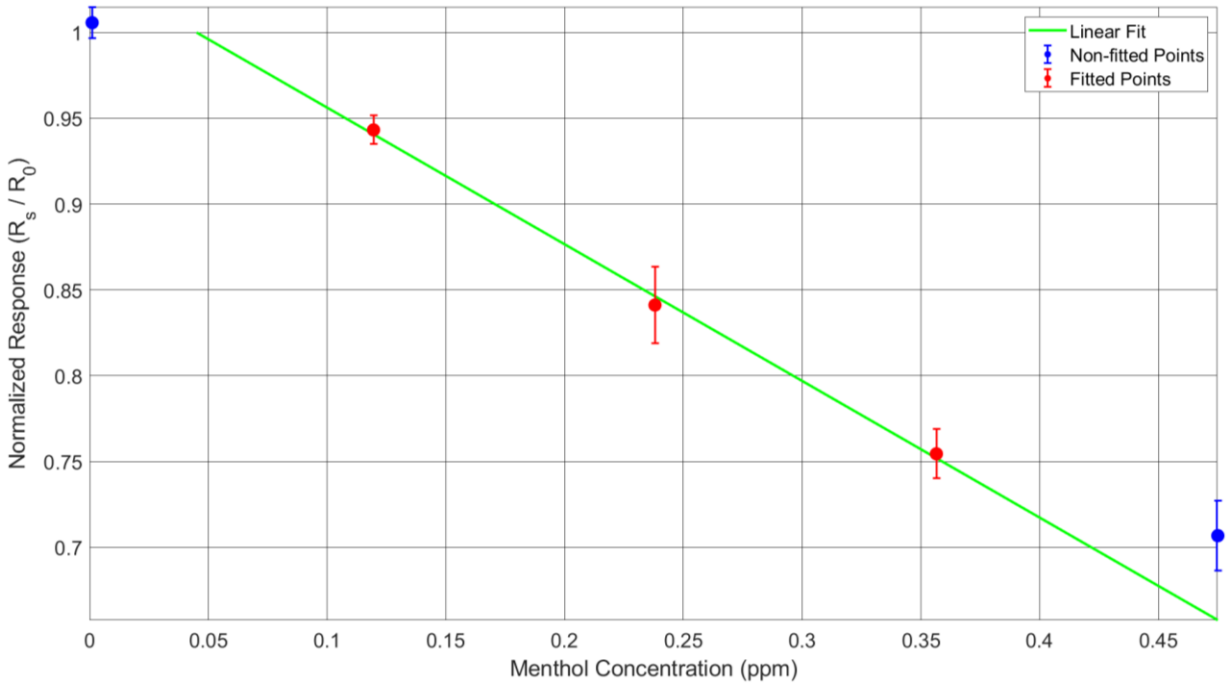

Figure 27: This figure shows the normalized response of the MICS 4514 Reducing Channel as a function of menthol concentration in ppm. The green line is the best-fit line of the linear response region given by the red points. The error bars indicate the range of three standard deviations in the observed response.

Figure 28: Calibration Plot of Sensor S000000029 (MICS 4514 Oxidizing Channel)

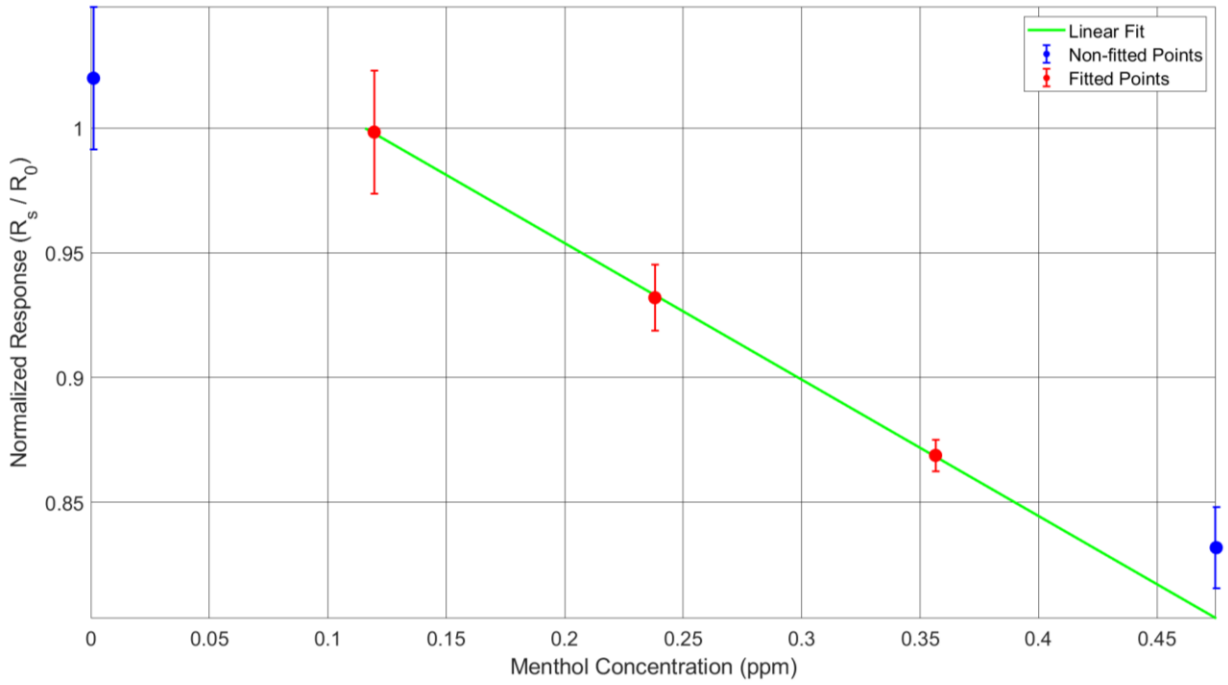

Figure 28: This figure shows the normalized response of the MICS 4514 Oxidizing Channel as a function of menthol concentration in ppm. The green line is the best-fit line of the linear response region given by the red points. The error bars indicate the range of three standard deviations in the observed response.

Figure 29: Calibration Plot of Sensor S000000030 (MICS 4514 Reducing Channel)

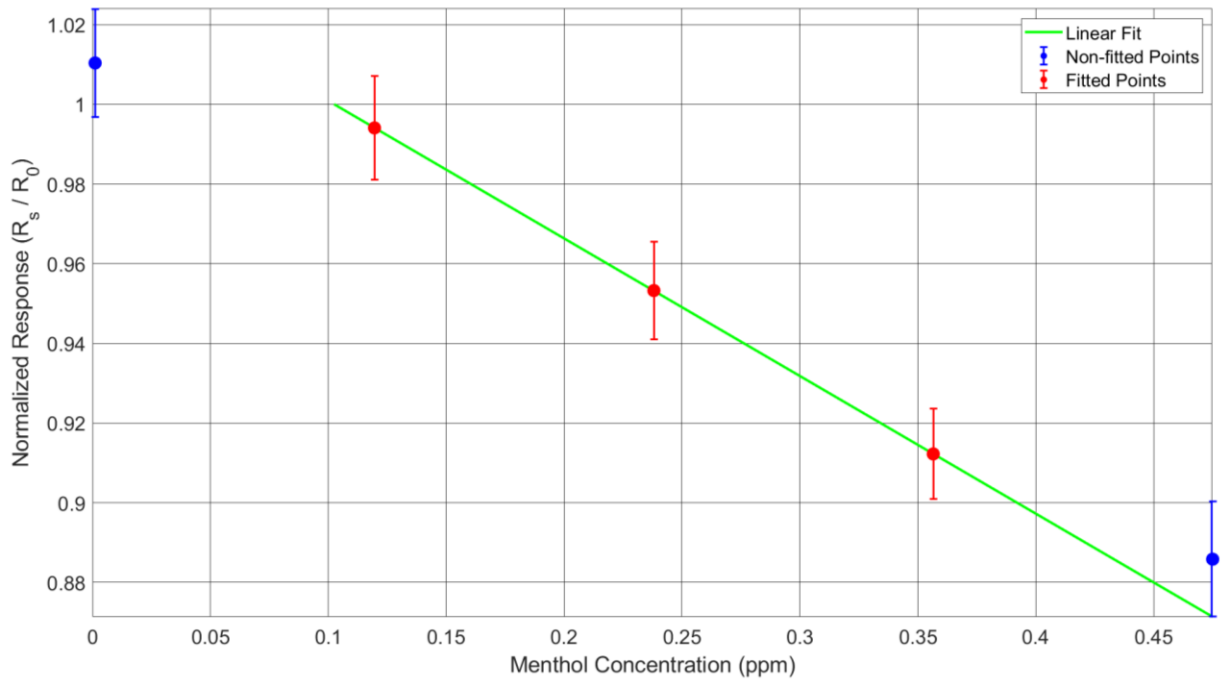

Figure 29: This figure shows the normalized response of the MICS 4514 Reducing Channel as a function of menthol concentration in ppm. The green line is the best-fit line of the linear response region given by the red points. The error bars indicate the range of three standard deviations in the observed response.

Figure 30: Calibration Plot of Sensor S000000031 (MICS 4514 Oxidizing Channel)

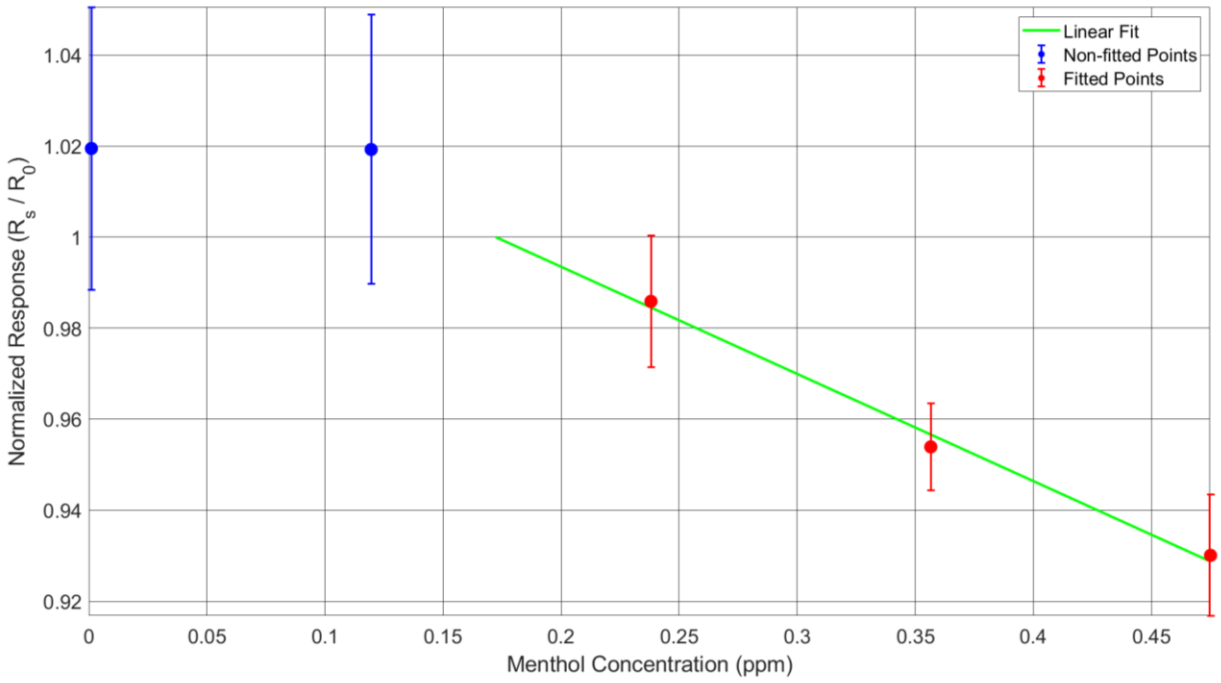

Figure 30: This figure shows the normalized response of the MICS 4514 Oxidizing Channel as a function of menthol concentration in ppm. The green line is the best-fit line of the linear response region given by the red points. The error bars indicate the range of three standard deviations in the observed response.

Figure 31: Calibration Plot of Sensor S000000036 (BME 680)

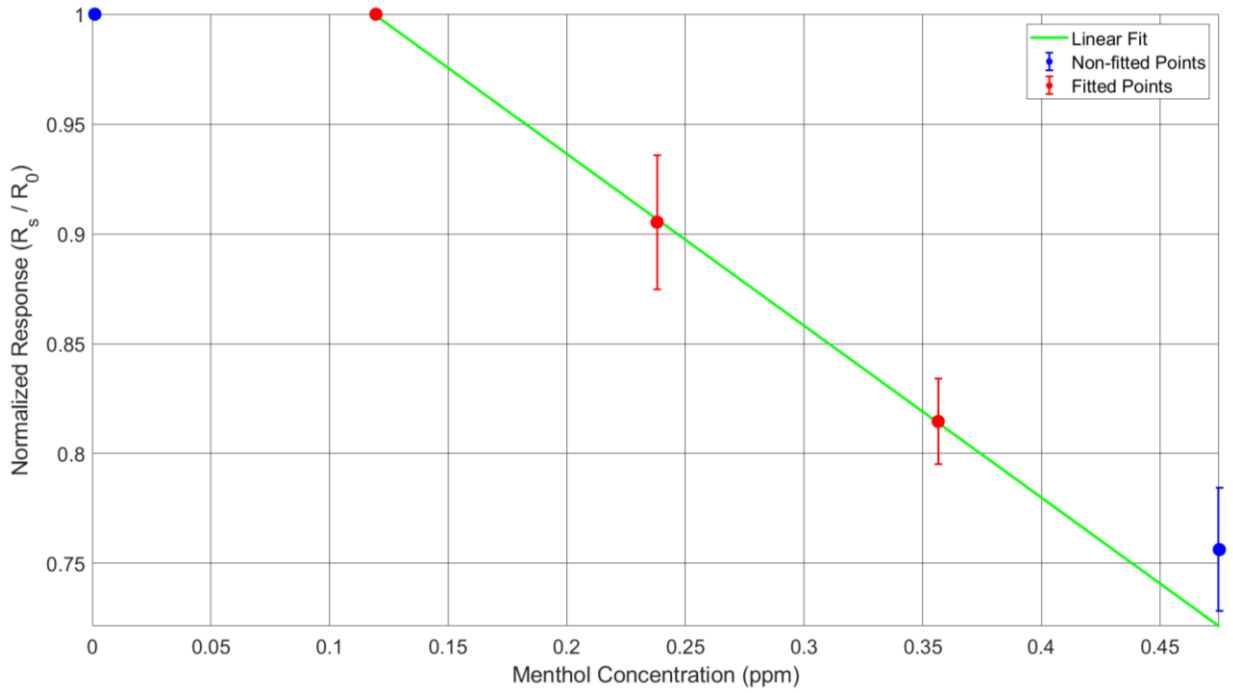

Figure 31: This figure shows the normalized response of the BME 680 as a function of menthol concentration in ppm. The green line is the best-fit line of the linear response region given by the red points. The error bars indicate the range of three standard deviations in the observed response.

Figure 32: Calibration Plot of Sensor S000000038 (TGS 2603)

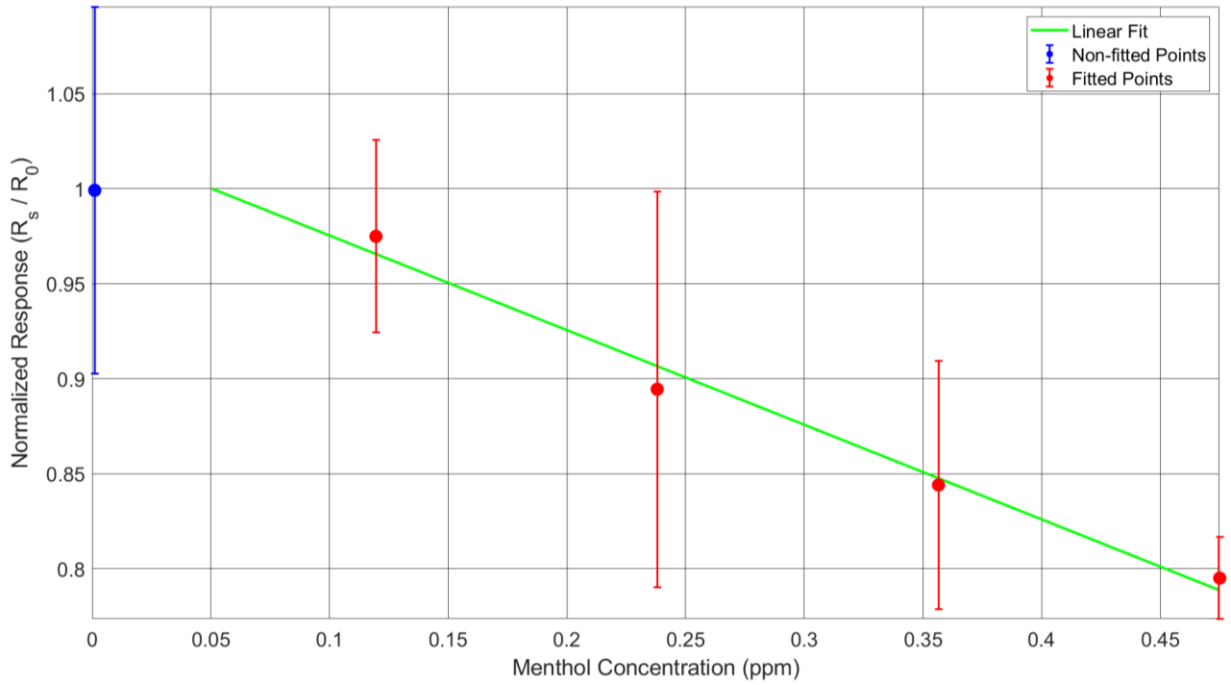

Figure 32: This figure shows the normalized response of the TGS 2603 as a function of menthol concentration in ppm. The green line is the best-fit line of the linear response region given by the red points. The error bars indicate the range of three standard deviations in the observed response.

VI. Tables

Table 1: List of Sensors Evaluated for Menthol Sensing

Sensor Model	Manufacturer	Sensor Identifier
FCM 2630	Figaro	S000000004
MICS 6814 (Reducing Channel)	Amphenol	S000000020
MICS 6814 (Oxidizing Channel)	Amphenol	S000000021
MICS 6814 (NH3 Channel)	Amphenol	S000000022
MICS 6814 (Reducing Channel)	Amphenol	S000000023
MICS 6814 (Oxidizing Channel)	Amphenol	S000000024
MICS 6814 (NH3 Channel)	Amphenol	S000000025
MICS 5524	Amphenol	S000000026
MICS 5524	Amphenol	S000000027
MICS 4514 (Reducing Channel)	Amphenol	S000000028
MICS 4514 (Oxidizing Channel)	Amphenol	S000000029
MICS 4514 (Reducing Channel)	Amphenol	S000000030
MICS 4514 (Oxidizing Channel)	Amphenol	S000000031
BME 680	Bosch	S000000036
BME 680	Bosch	S000000037
TGS 2603	Figaro	S000000038
TGS 832-A00	Figaro	S000000040
TGS 832-A00	Figaro	S000000041
TGS 3830	Figaro	S000000044

Table 2: Menthol Exposure Sequence

Step Number	Menthol Concentration in Air (ppm mol/mol)	Exposure Duration (hours)
1	0	36
2	0.0011	1
3	0	4
4	0.0011	1
5	0	4
6	0.0011	1
7	0	4
8	0.12	1
9	0	4
10	0.12	1
11	0	4
12	0.12	1
13	0	4
14	0.24	1
15	0	4

16	0.24	1
17	0	4
18	0.24	1
19	0	4
20	0.36	1
21	0	4
22	0.36	1
23	0	4
24	0.36	1
25	0	4
26	0.48	1
27	0	4
28	0.48	1
29	0	4
30	0.48	1
31	0	4

Table 3: Sensor Response Characteristics

Sensor Identifier	Response Observed?	Normalized Linear Sensitivity (ppm^{-1})	Minimum Concentration of LR (ppm)	Maximum Concentration of LR (ppm)	Extrapolated Menthol LLOD (ppm)
S000000004	None	NC	NC	NC	NC
S000000020	Strong	0.703	0.12	0.36	0.051
S000000021	Weak	NC	NC	NC	NC
S000000022	Strong	0.971	0.12	0.48	0.089
S000000023	Weak	NC	NC	NC	NC
S000000024	Weak	NC	NC	NC	NC
S000000025	Weak	NC	NC	NC	NC
S000000026	Strong	-0.706	0.12	0.36	0.061
S000000027	Strong	-0.330	0.12	0.36	0.014
S000000028	Strong	-0.796	0.12	0.36	0.045
S000000029	Strong	-0.547	0.12	0.36	0.12
S000000030	Strong	-0.345	0.12	0.36	0.10
S000000031	Strong	-0.236	0.24	0.48	0.17
S000000036	Strong	-0.782	0.12	0.36	0.12
S000000037	None	NC	NC	NC	NC
S000000038	Strong	-0.498	0.12	0.48	0.050
S000000040	None	NC	NC	NC	NC
S000000041	None	NC	NC	NC	NC
S000000044	None	NC	NC	NC	NC

References

(1) Shahid, M.; Lee, M. Y.; Yeon, A.; Cho, E.; Sairam, V.; Valdiviez, L.; You, S.; Kim, J. Menthol, a Unique Urinary Volatile Compound, Is Associated with Chronic Inflammation in Interstitial Cystitis. *Sci Rep* **2018**, *8* (1), 10859. https://doi.org/10.1038/s41598-018-29085-3.

(2) Bochenkov, V. E.; Sergeev, G. B. Sensitivity, Selectivity, and Stability of Gas-Sensitive Metal-Oxide Nanostructures. In *Metal Oxide Nanostructures and Their Applications*; Umar, A., Hahn, Y.-B., Eds.; American Scientific Publishers, 2010; Vol. 3, pp 31–52.

(3) Franke, M. E.; Koplin, T. J.; Simon, U. Metal and Metal Oxide Nanoparticles in Chemiresistors: Does the Nanoscale Matter? *Small* **2006**, *2* (1), 36–50. https://doi.org/10.1002/smll.200500261.

(4) Ji, H.; Zeng, W.; Li, Y. Gas Sensing Mechanisms of Metal Oxide Semiconductors: A Focus Review. *Nanoscale* **2019**, *11* (47), 22664–22684. https://doi.org/10.1039/C9NR07699A.

(5) Gründler, P. *Chemical Sensors: An Introduction for Scientists and Engineers*; Springer: Berlin ; New York, 2007.

(6) Eranna, G. *Metal Oxide Nanostructures as Gas Sensing Devices*; CRC Press/Taylor & Francis: Boca Raton, 2012.

(7) Štejfa, V.; Bazyleva, A.; Fulem, M.; Rohlíček, J.; Skořepová, E.; Růžička, K.; Blokhin, A. V. Polymorphism and Thermophysical Properties of L- and Dl-Menthol. *The Journal of Chemical Thermodynamics* **2019**, *131*, 524–543. https://doi.org/10.1016/j.jct.2018.11.004.

(8) Smith, J. M.; Van Ness, H. C.; Abbott, M. M.; Swihart, M. T. *Introduction to Chemical Engineering Thermodynamics*, Eighth edition.; McGraw-Hill Education: New York, NY, 2018; pp. 605 – 606.

(9) Zhang, T.; Nix, M. B.; Yoo, B.-Y.; Deshusses, M. A.; Myung, N. V. Electrochemically Functionalized Single-Walled Carbon Nanotube Gas Sensor. *Electroanalysis* **2006**, *18* (12), 1153–1158. https://doi.org/10.1002/elan.200603527.

(10) Korotcenkov, G.; Cho, B. K. Instability of Metal Oxide-Based Conductometric Gas Sensors and Approaches to Stability Improvement (Short Survey). *Sensors and Actuators B: Chemical* **2011**, *156* (2), 527–538. https://doi.org/10.1016/j.snb.2011.02.024.

(11) Kim, S.; Brady, J.; Al-Badani, F.; Yu, S.; Hart, J.; Jung, S.; Tran, T.-T.; Myung, N. V. Nanoengineering Approaches Toward Artificial Nose. *Front. Chem.* **2021**, *9*, 629329. https://doi.org/10.3389/fchem.2021.629329.

Appendix A: Table of Nomenclature

Abbreviation	Meaning
°C	Degrees celsius
K	Kelvin
LLOD	Lower limit of detection
LR	Linear response
NC	Not calculated
P	Pressure
P_A	Partial pressure of component A
Pa	Pascal
ppb	Parts per billion
ppm	Parts per million
$P_{vp,A}$	Vapor pressure of component A
$P_{vp,m}$	Vapor pressure of menthol
R_0	Baseline resistance
R_s	Sensor resistance
sccm	Standard cubic centimeter per minute
T	Temperature
y_A	Vapor-phase mole fraction of component A